Heliyon 10 (2024) e24005

Contents lists available at ScienceDirect

Heliyon

journal homepage: www.cell.com/heliyon

Discovery of new thiazolidine-2,4-dione derivatives as potential VEGFR-2 inhibitors: *In vitro* and *in silico* studies

Ibrahim H. Eissa [a,**], Hazem Elkady [a,*], Mahmoud Rashed [a], Alaa Elwan [a], Mohamed Hagras [b], Mohammed A. Dahab [a], Mohammed S. Taghour [a], Ibrahim M. Ibrahim [c], Dalal Z. Husein [d], Eslam B. Elkaeed [e], Hanan A. Al-ghulikah [f], Ahmed M. Metwaly [g], Hazem A. Mahdy [a,***]

[a] *Pharmaceutical Medicinal Chemistry & Drug Design Department, Faculty of Pharmacy (Boys), Al-Azhar University, Cairo, 11884, Egypt*
[b] *Department of Pharmaceutical Organic Chemistry, College of Pharmacy, Al-Azhar University, Cairo, 11884, Egypt*
[c] *Biophysics Department, Faculty of Science, Cairo University, Giza, 12613, Egypt*
[d] *Chemistry Department, Faculty of Science, New Valley University, El-Kharja, 72511, Egypt*
[e] *Department of Pharmaceutical Sciences, College of Pharmacy, AlMaarefa University, Riyadh, 13713, Saudi Arabia*
[f] *Department of Chemistry, College of Science, Princess Nourah bint Abdulrahman University, P.O. Box 84428, Riyadh 11671, Saudi Arabia*
[g] *Pharmacognosy and Medicinal Plants Department, Faculty of Pharmacy (Boys), Al-Azhar University, Cairo, 11884, Egypt*

ARTICLE INFO

Keywords:
Drug design
VEGFR-2 inhibitors
Anticancer
Thiazolidine-2,4-dione
In silico studies

ABSTRACT

In this study, a series of seven novel 2,4-dioxothiazolidine derivatives with potential anticancer and VEGFR-2 inhibiting abilities were designed and synthesized as VEGFR-2 inhibitors. The synthesized compounds were tested *in vitro* for their potential to inhibit VEGFR-2 and the growth of HepG2 and MCF-7 cancer cell lines. Among the compounds tested, compound **22** ($IC_{50} = 0.079$ μM) demonstrated the highest *anti*-VEGFR-2 efficacy. Furthermore, it demonstrated significant anti-proliferative activities against HepG2 ($IC_{50} = 2.04 \pm 0.06$ μM) and MCF-7 ($IC_{50} = 1.21 \pm 0.04$ M). Additionally, compound **22** also increased the total apoptotic rate of the MCF-7 cancer cell lines with cell cycle arrest at S phase. As well, computational methods were applied to study the VEGFR-2-**22** complex at the molecular level. Molecular docking and molecular dynamics (MD) simulations were used to investigate the complex's structural and kinetic characteristics. The DFT calculations further revealed the structural and electronic properties of compound **22**. Finally, computational ADMET and toxicity tests were performed indicating the likeness of the proposed compounds to be drugs. The results suggest that compound **22** displays promise as an effective anticancer treatment and can serve as a model for future structural modifications and biological investigations in this field.

* Corresponding author. Medicinal Chemistry Department, Faculty of Pharmacy (Boys), Al-Azhar University, Cairo, 11884, Egypt.
** Corresponding author. Medicinal Chemistry Department, Faculty of Pharmacy (Boys), Al-Azhar University, Cairo, 11884, Egypt.
*** Corresponding author. Medicinal Chemistry Department, Faculty of Pharmacy (Boys), Al-Azhar University, Cairo, 11884, Egypt.
E-mail addresses: Ibrahimeissa@azhar.edu.eg (I.H. Eissa), Hazemelkady@azhar.edu.eg (H. Elkady), mahmoudsayed.222@azhar.edu.eg (M. Rashed), alaaelwan34@azhar.edu.eg (A. Elwan), m.hagrs@Azhar.edu.eg (M. Hagras), mohammeddahab@azhar.edu.eg (M.A. Dahab), mohammad1533.el@azhar.edu.eg (M.S. Taghour), ibrahim_mohamed@cu.edu.eg (I.M. Ibrahim), dalal_husein@sci.nvu.edu.eg (D.Z. Husein), ekaeed@um.edu.sa (E.B. Elkaeed), haalghulikah@pnu.edu.sa (H.A. Al-ghulikah), ametwaly@azhar.edu.eg (A.M. Metwaly), hazem_hady2001@azhar.edu.eg (H.A. Mahdy).

https://doi.org/10.1016/j.heliyon.2024.e24005
Received 6 October 2023; Received in revised form 12 December 2023; Accepted 2 January 2024
Available online 12 January 2024

1. Introduction

Cancer stands as one of the most formidable and pervasive challenges confronting human health worldwide [1]. Its multifaceted nature, diverse manifestations, and impact on individuals and communities underscore the urgency for continued research, innovation, and targeted therapeutic interventions [2–6]. One of the most crucial targets in cancer treatment is angiogenesis, the process of forming new blood vessels. It plays a pivotal role in the spread of cancer and is considered a hallmark of various types of cancer [7]. Angiogenesis driven by the activation of various signaling systems that facilitate the creation of new blood capillaries from existing vasculature [8]. In the context of tumor angiogenesis, tyrosine kinases (TKs), particularly VEGFR-2, are key regulators. VEGFR-2, which is often over-expressed in cancer cells, triggers a series of downstream signals that enhance the angiogenesis and potentiate cancer cell survival, growth, and proliferation [9]. Consequently, inhibiting or reducing VEGFR-2 signaling has become a crucial strategy in the quest for novel treatments for angiogenesis-dependent malignancies [9–11]. Numerous experimental cancer models have demonstrated the ability of thiazolidine-2,4-diones (TZDs) to inhibit tumor angiogenesis, alter the cell cycle, induce cell differentiation, and promote apoptosis, in addition to their known anticancer effects [12,13]. Through *in vitro* models, TZD derivatives have been shown to effectively inhibit angiogenesis and act as anticancer agents by targeting VEGFR-2 and reducing VEGF synthesis [14]. Given its pivotal role in angiogenesis, VEGFR-2 remains a critical target for anti-angiogenic cancer treatment. Several potent VEGFR-2 inhibitors, including Sunitinib and Sorafenib, have been developed and approved for antiangiogenic therapy in various malignancies [15,16]. Building on our prior research in designing VEGFR-2 inhibitors [17–21], this study introduces a novel series of thiazolidine-2,4-dione derivatives. These compounds were developed and synthesized based on the primary pharmacophoric characteristics of VEGFR-2 inhibitors.

1.1. Rational

VEGFR-2 inhibitors are a group of small molecules that bind to the ATP-binding region of the receptor and prevent lymphangiogenesis and angiogenesis [22]. Although the FDA has approved a number of VEGFR-2 inhibitors, significant research is still

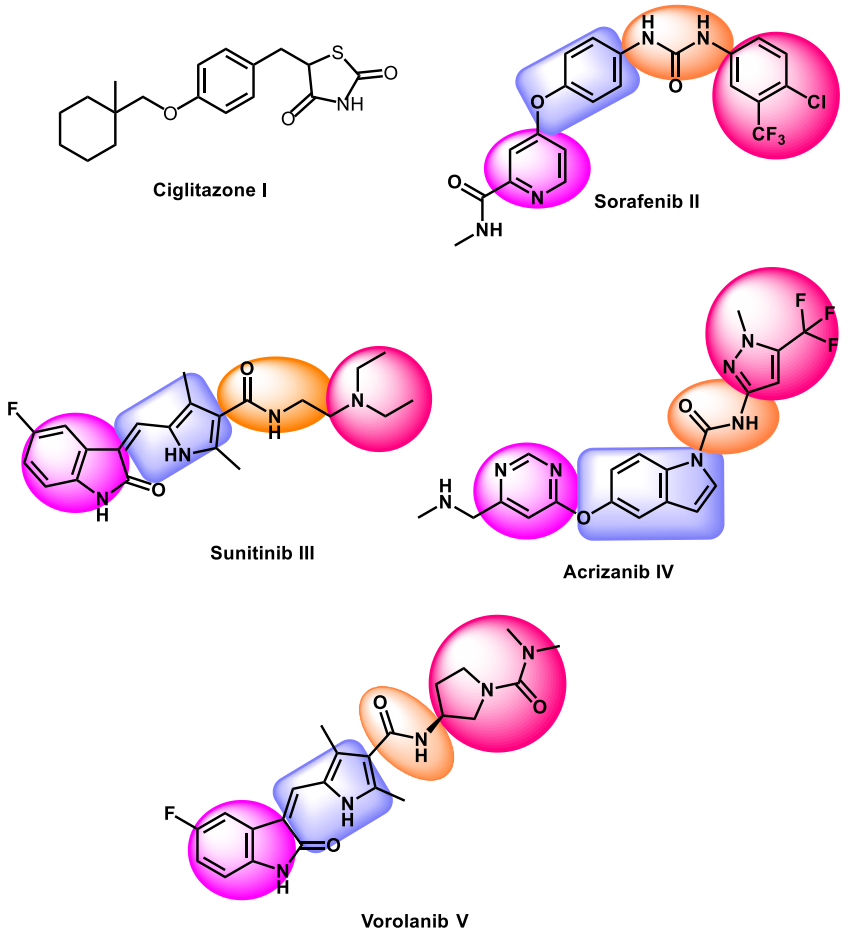

Fig. 1. Some reported VEGF and VEGFR-2 inhibitors with their basic pharmacophoric features.

being done to find new VEGFR-2 inhibitors in order to circumvent the limitations of currently prescribed medications. A pyridine derivative known as sorafenib **II** effectively inhibits VEGFR-2 [23]. A derivative of isatin called sunitinib **III** has the potential to be anticancer and has dual inhibitory effect against PDGFR and VEGFR-2 [24]. The indole derivative acirizanib **IV** exhibits a potent VEGFR-2 inhibitory action with minimal systemic exposure [25]. Through the suppression of VEGFR-2, the isatin derivative vorolanib **V** shows good tumor-inhibitory effects [26]. It has less side effects and a broad range of activity [27] (Fig. 1).

VEGFR-2 inhibiting drugs have some pharmacophoric structural features that are essential for binding with the ATP binding inside the VEGFR-2 binding site [3,28–32]. The features comprise a hetero aromatic structure that occupy the hinge region of the active site to form an essential hydrogen bandwith Cys917 [29]. In addition, the features should involve a spacer moiety to occupy the area between the hinge region and the DFG domain [33]. Furthermore, a very essential moiety called pharmacophore should be included in the VEGFR-2 inhibitors to occupy the DFG motif region. The pharmacophore moiety should contain at least one hydrogen bond acceptor (HBA) and one hydrogen bond donor (HBD) groups. The hydrogen bond forming groups have a critical role through the formation of hydrogen bonding interactions Glu883 and Asp1044 [34]. Lastly, the panel of pharmacophoric features should comprise a

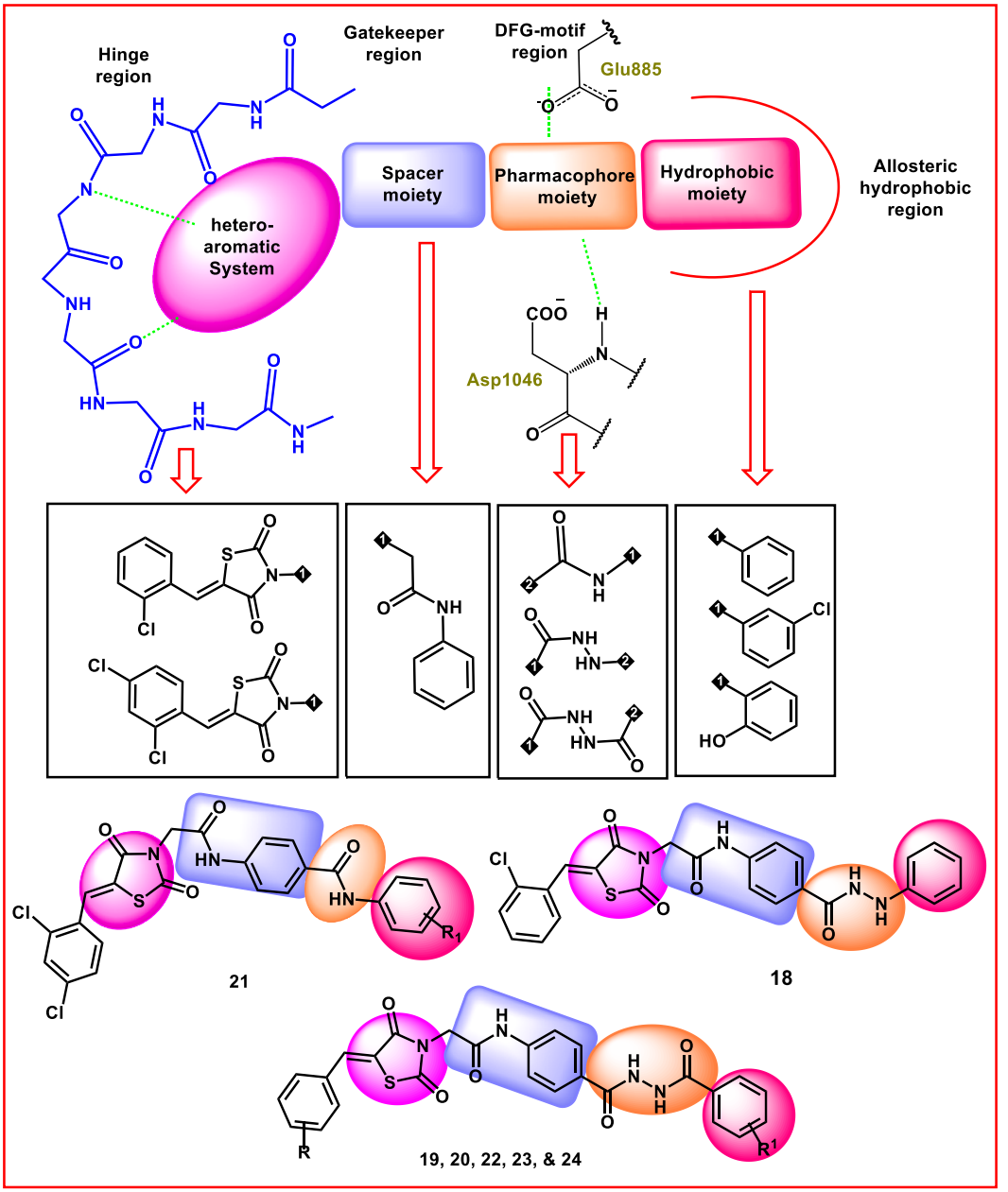

Fig. 2. Strategy of molecular design of the new VEGFR-2 inhibitors.

hydrophobic tail to occupy allosteric hydrophobic pocket of VEGFR-2 forming many hydrophobic interactions [35] (Figs. 1 and 2).

In this work, we aimed at the design of new molecules that have the pharmacophoric features of VEGFR-2 inhibitors depending on a ligand-based drug design approach [36–39]. As shown in Fig. 2, different chemically active moieties were utilized to generate new compounds that can accommodate easily in the active pocket of VEGFR-2. At first, two (*Z*)-5-benzylidenethiazolidine-2,4-dione derivatives were used to act as hetero-aromatic systems and capable of occupying the hinge region of the active site. These derivatives are (*Z*)-5-(2-chlorobenzylidene)thiazolidine-2,4-dione and (*Z*)-5-(2,4-dichlorobenzylidene)thiazolidine-2,4-dione. Then, *N*-phenyl-acetamide moiety was tended to attach the (*Z*)-5-benzylidenethiazolidine-2,4-dione derivatives to act as a linker moiety and occupy the gatekeeper site. Next, three functional groups were used as a pharmacophore moiety. These groups are amide, hydrazide, and diamide moieties. Each of them has at least one HBA and one HBD atoms to form hydrogen bonding with Glu883 and Asp1044 inside the DFG motif. Finally, variety of substituted phenyl rings represent the hydrophobic tail to be inoculated in the allosteric pocket of the active site.

2. Results and discussion

2.1. Chemistry

The synthetic strategy employed to synthesize the desired 5-benzylidenethiazolidine-2,4-dione derivatives **18**–**24** was represented in Schemes 1, **2**, **3**, and **4**. The benzylidene intermediates **5a**,**b** were synthesized by reacting different aldehydes **4a**,**b** with thiazolidine-2,4-dione **3** in dry toluene in presence of piperidine. Subsequently, derivatives **5a**,**b** were converted into the corresponding potassium salts **6a**,**b** by the reaction with potassium hydroxide in ethanolic medium (Scheme 1).

The key intermediates **11, 13,** and **17a-c** were then synthesized through multiple steps; firstly, 4-(2-chloroacetamido)benzoic acid **8** underwent an an acylation reaction with thionyl chloride in the presence of a catalytic amount of *N*,*N*-dimethylformamide to give 4-(2-chloroacetamido)benzoyl chloride **9**. In the second step, the derivative **9** was allowed to react with different amine derivatives namely, phenyl hydrazine **10**, 3-chloroaniline **12** and benzohydrazides **16a-c** to afford the key intermediate **11, 13,** and **17a-c**, respectively (Scheme 2).

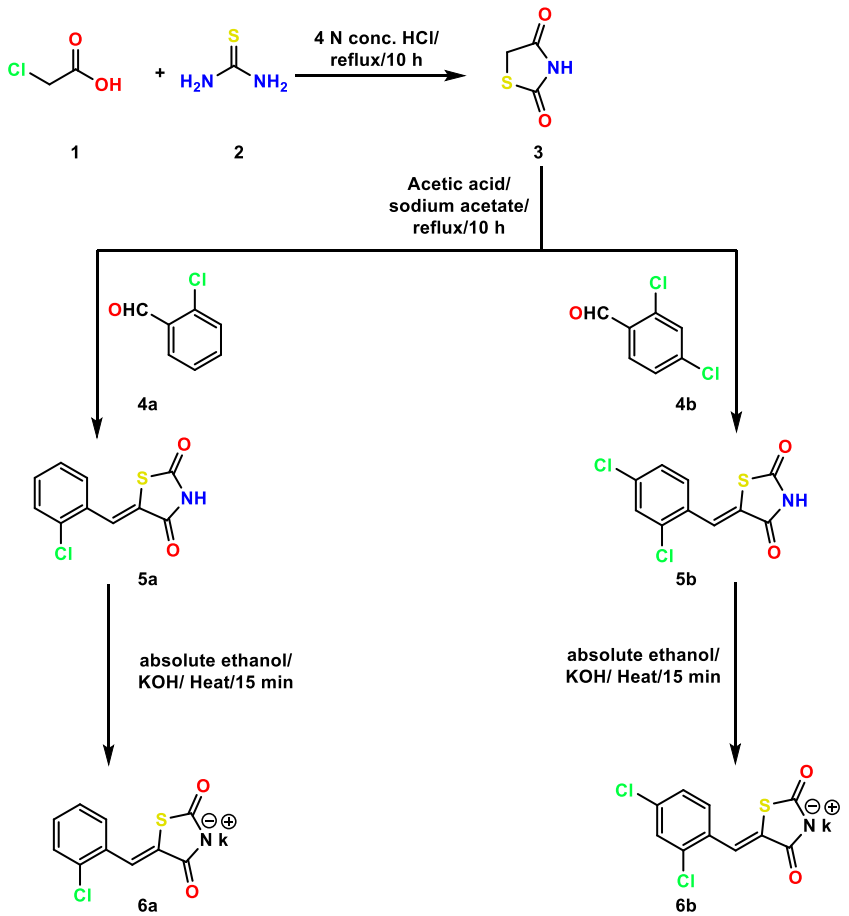

Scheme 1. Synthesis of the key starting materials **6a**,**b**.

Finally, the target compounds **18**–**24** were obtained, with good yields ranging from 65 to 86 %, by reacting potassium salts (**6a**,**b**) with the key intermediate **11, 13,** and **17a-c** in refluxing DMF (Schemes 3 and 4).

The target 5-benzylidenethiazolidine-2,4-dione derivatives **18**–**24** were confirmed structurally by elemental and spectral analyses. The ^{1}H NMR spectra revealed singlet signals around δ 10.97–10.31 ppm for the protons of the NH groups in all compounds. Furthermore, singlet signals for benzylidine and methylene protons in the range of δ 8.12–8.03 ppm and δ 4.63–4.61 ppm, respectively were noticed in all compounds. In addition, ^{1}H NMR spectra for derivatives **20** and **24** showed another singlet signal for the OH group at δ 11.93 and δ 11.90 ppm, respectively. Moreover, ^{13}C NMR spectra confirmed the presence of the carboxylic C═O functionalities at the range of δ 168.25–164.67 ppm for the target derivatives. Furthermore, ^{13}C NMR spectra for all compounds showed a signal at δ 44.78–44.74 ppm for the methylene carbon.

2.2. Biological evaluation

2.2.1. In-vitro anticancer effects

The MTT assay was used to explore the anti-proliferative properties of the target thiazolidine-2,4-dione derivatives **18**–**24** against two tumor cell lines (HepG2 and MCF-7) [40]. Sorafenib, a reference cytotoxic drug, was applied in this experiment. The cytotoxicity outcomes was shown in Table 1 and expressed as IC_{50} values. Generally, all the tested members demonstrated promising cytotoxic activities ranging from 0.60 to 4.70 μM against HepG2 and MCF-7 cell lines.

In details, all the tested members exhibited cytotoxic effects on MCF-7 (IC_{50} values ranging from 0.65 to 2.29 μM) that were superior to those of sorafenib ($IC_{50} = 3.17 \pm 0.01$ μM). As well, compounds **20** ($IC_{50} = 1.14 \pm 0.03$ μM), **21** ($IC_{50} = 0.84 \pm 0.01$ μM), **22**

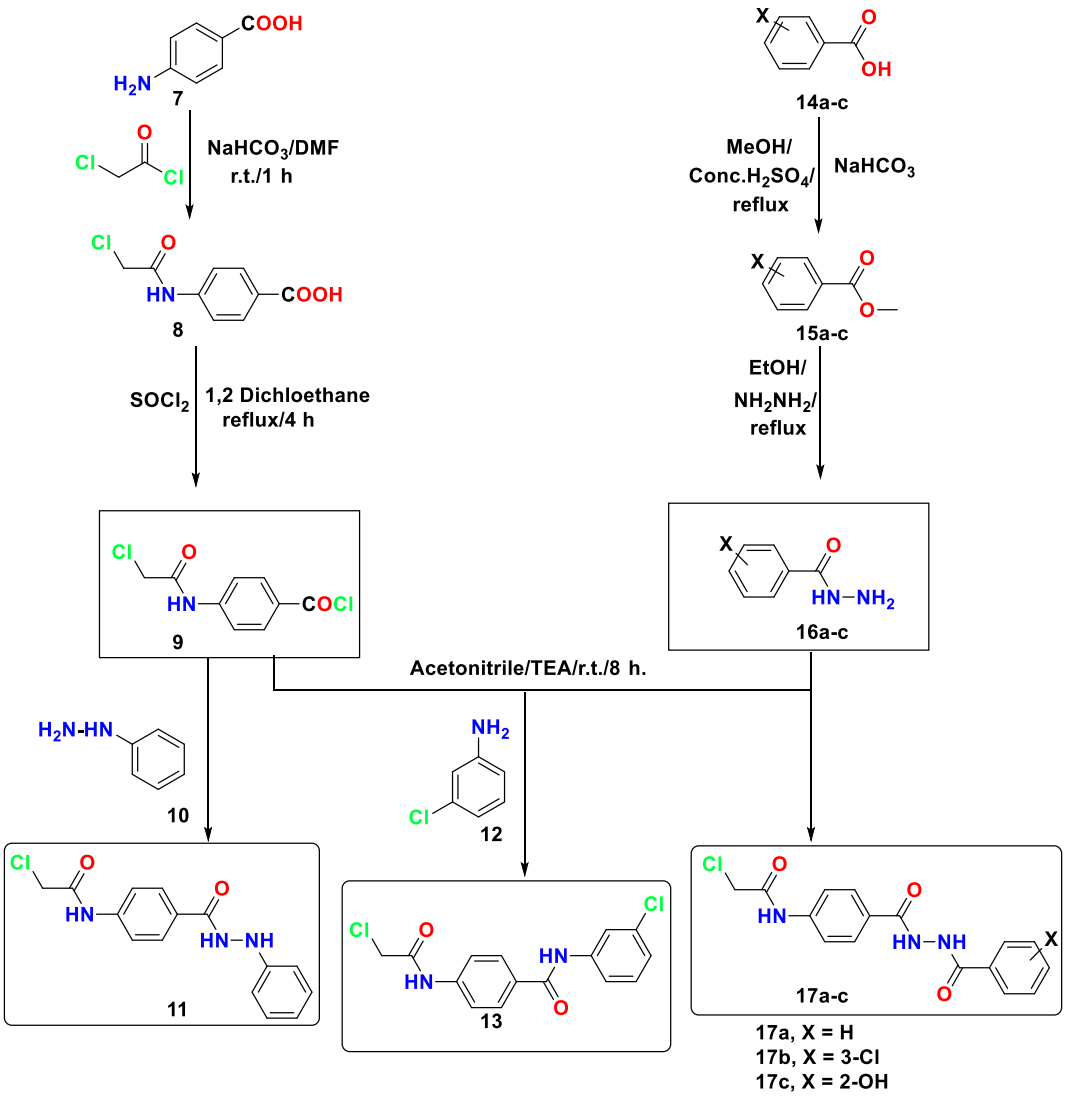

Scheme 2. Synthesis of the key intermediates **11, 13,** and **17a-c**.

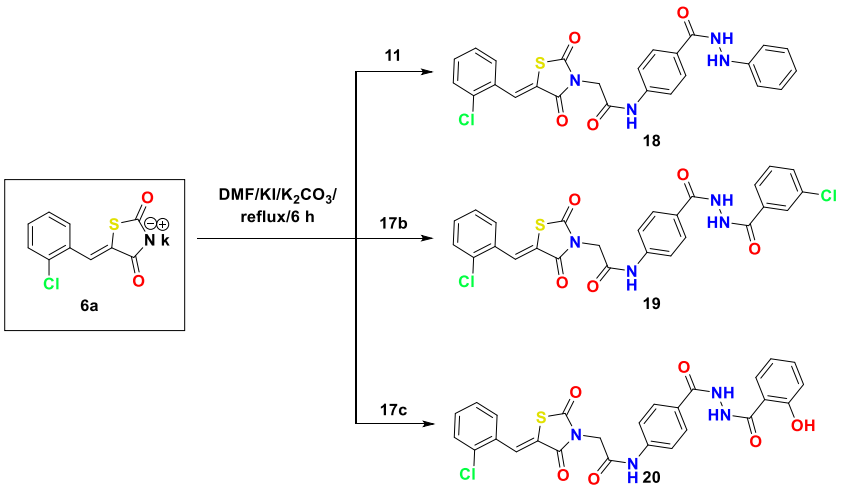

Scheme 3. Synthesis of the target compounds **18**–**20**.

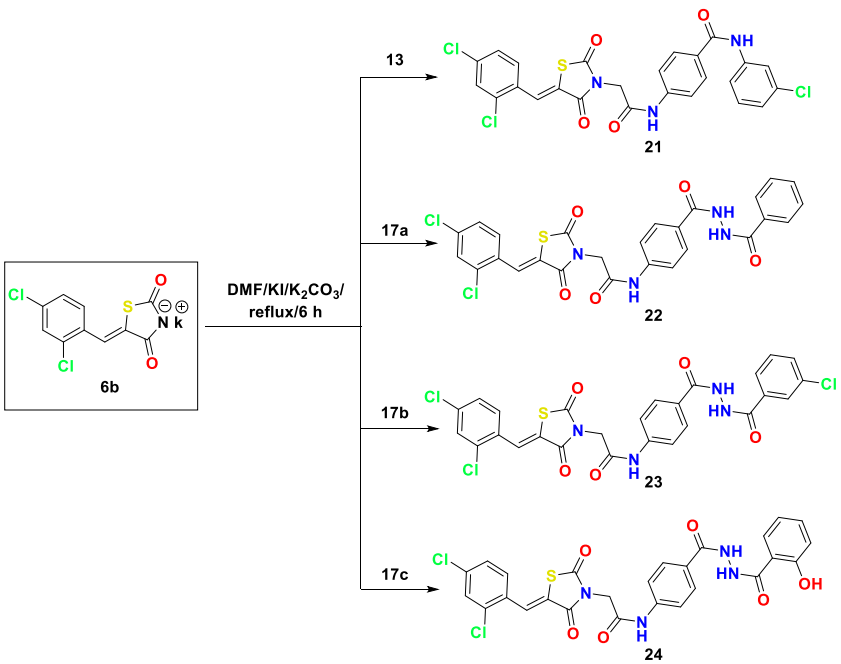

Scheme 4. Synthesis of the target compounds **21**–**24**.

Table 1
In vitro cytotoxic and inhibitory activities of the target compounds against HepG2 and MCF-7 cell lines.

Comp.	HepG2 IC_{50} (μM)[a]	MCF-7 IC_{50} (μM)[a]
18	4.7 ± 0.1	1.76 ± 0.02
19	3.06 ± 0.02	2.29 ± 0.19
20	1.14 ± 0.03	0.66 ± 0.03
21	0.84 ± 0.01	0.68 ± 0.01
22	2.04 ± 0.06	1.21 ± 0.04
23	1.18 ± 0.01	0.95 ± 0.01
24	0.6 ± 0.02	0.65 ± 0.01
Sorafenib	2.24 ± 0.06	3.17 ± 0.01

[a] The results are the mean of three experiments.

(IC_{50} = 2.04 ± 0.06 μM**), 23 (**IC_{50} = 1.18 ± 0.01 μM**),** and **24** (IC_{50} = 0.6 ± 0.02 μM) showed cytotoxic activities against HepG2 surpassing that of sorafenib (IC_{50} = 2.24 ± 0.06 μM).

2.2.2. *In vitro VEGFR-2 enzyme assay inhibition*

The potential of the thiazolidine-2,4-dione derivatives **18**–**24** to inhibit VEGFR-2 was the main focus of our work. The positive control in this experiment was sorafenib. To express and assemble the findings of VEGFR-2 inhibition, growth inhibitory concentration (IC_{50}) values were employed (Table 2).

The strongest VEGFR-2 inhibitor in this study was compound **22**, as seen in Table 2. Its IC_{50} value of 0.079 ± 0.003 μM was comparable to that of sorafenib (IC_{50} = 0.046 ± 0.002 μM). Next, compounds **19** (IC_{50} = 0.323 ± 0.014 μM), **20** (IC_{50} = 0.21 ± 0.009 μM), **23** (IC_{50} = 0.328 ± 0.014 μM), **24** (IC_{50} = 0.203 ± 0.009 μM) showed good VEGFR-2 inhibitory activity. Finally, compounds **18** (IC_{50} = 2.661 ± 0.112 μM) and **21** (IC_{50} = 1.662 ± 0.07 μM) revealed moderate inhibitory actions against VEGFR-2.

2.2.3. *Structure-activity relationship (SAR)*

Depending the results of VEGFR-2 inhibitory activities, we can catch a valuable SAR. First, the effect of substitution on (*Z*)-5-benzylidenethiazolidine-2,4-dione moiety with mono-chloro and di-chloro atoms. Comparing the activity of compounds **20** (IC_{50} = 0.210 ± 0.009 μM) with that of compound **24** (IC_{50} = 0.203 ± 0.009 μM), and the activity of compound **19** (IC_{50} = 0.323 ± 0.014 μM) with that of compound **23** (IC_{50} = 0.328 ± 0.014 μM), it was observed that the activities of each pairs of compound are almost the same. This indicated that the substitution with mono-chloro or di-chloro atoms has non-significant effect on the VEGFR-2 inhibitory activities.

Then, the effect of different pharmacophore moieties was investigated. Observing the activity of compounds **21** (incorporating an amide moiety, IC_{50} = 1.662 ± 0.07 μM), **23** (incorporating a diamide moiety, IC_{50} = 0.328 ± 0.014 μM), and **18** (incorporating a hydrazide amide moiety, IC_{50} = 2.661 ± 0.112 μM), indicated that compound **21** more active than compound **23**, and the latter is more active than compound **18**. This revealed that the positive effect of the pharmacophore moieties can be arranged descendingly as amide > diamide > hydrazide.

Next, the effect of the substitution on the terminal phenyl ring (hydrophobic tail) was examined. The unsubstituted phenyl-containing compound **22** (IC_{50} = 2.661 ± 0.112 μM) showed a higher activity than the hydroxyl phenyl-containing compound **24** (IC_{50} = 0.203 ± 0.009 μM). The latter exhibited a higher activity than the chloro phenyl-containing compound **23** (IC_{50} = 0.328 ± 0.014 μM). These findings indicated the unsubstituted phenyl ring may give a higher activity than the substituted phenyl ring with electron donating group, which may produce a higher activity than the substituted phenyl ring with electron withdrawing group (H > OH > Cl) (Fig. 3).

2.2.4. *In vitro safety assay (selectivity index)*

The selectivity of anticancer agents toward the cancer cells is a crucial issue during the discovery of new active agent [41]. Therefore, the toxicity of the most promising compound **22** against normal (Vero) and its selectivity against tumor cells was evaluated (Table 2).

Compound **22** showed a low toxicity against normal cells showing an IC_{50} value of 3.97 ± 0.05 μM. To calculate the selectivity indices of compound **22** toward HepG2 and MCF-7, The IC_{50} value against Vero cells was divided on both the IC_{50} values against HepG2 and MCF-7 cells. The results revealed that compound **22** has a higher selectivity toward MCF-7 (3.28) than HepG2 (1.95).

2.2.5. *Cell cycle analysis*

Eukaryotic cells undergo a well regulated process of replication through a succession of cell cycles. Anti-proliferative drugs inhibit one or more cell cycle checkpoints, which can result in cell cycle arrest and the activation of apoptosis. This slows the development of cancer cells. Finding the precise cell cycle stages at which arrest occurs is a vital step in the development of novel medications for the treatment of cancer [42].

In the current study, 1.21 μM (IC_{50}) of compound **22** was added to MCF-7 cells, and the cell cycle was then examined for any variations in comparison to untreated MCF-7 cells. The findings demonstrated that compound **22** triggered stop in MCF-7 cell growth in the S phase (Table 3, Fig. 4, and Fig. S1). Precisely, compound **22** significantly reduced the percentage of MCF-7 cells in the G2/M

Table 2
In vitro inhibitory activities of the thiazolidine-2,4-dione derivatives **18**–**24** against VEGFR-2.

Comp.	*In vitro* VEGFR-2 IC_{50} (μM)[a]
18	2.661 ± 0.112
19	0.323 ± 0.014
20	0.21 ± 0.009
21	1.662 ± 0.07
22	0.079 ± 0.003
23	0.328 ± 0.014
24	0.203 ± 0.009
Sorafenib	1.46 0.002

[a] The results are the mean of three experiments.

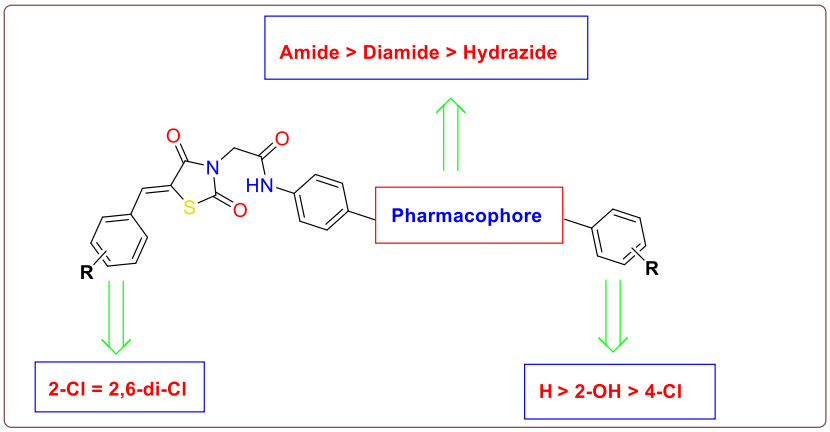

Fig. 3. SAR studies of the synthesized compounds as VEGFR-2 inhibitors.

stage (from 16.35 % to 13.77 %) and G0-G1 stage (from 59.04 % to 52.39 %), while significantly increased the cell population at the S phase (from 24.61 % to 33.84 %). This test demonstrated compound **22**'s ability to stop the cell cycle at the S phase.

2.2.6. *Apoptosis induction*

The Annexin-V/propidium iodide staining test was employed to assess the apoptotic effect of compound **22** at a dosage of 1.21 μM on MCF-7 cells. Table 4, Fig. 5, and Fig. S2 showed that compound **22** significantly increased both early and late apoptosis in MCF-7 cells, with percentages of 22.15 % and 13.53 %, respectively, compared to untreated cells at 0.29 % and 0.15 %. This indicates that compound **22** can upsurge early apoptosis in MCF-7 cells by about 76 times and late apoptosis by about 90-fold when compared to untreated cells.

2.2.7. *The effect of compound 22 on MCF-7's migration and healing*

A wound healing is an additional technique used in this study to evaluate the effect of compound **22** on the migration and healing of MCF-7 cancer cells. In this *in vitro* method, a scratch was made on a monolayer of MCF-7 cancer cells, its initial diameter was measured, and its closure was observed for both treated and untreated cells at specified intervals (0, 24, and 48 h). The pictures of the scratch areas on treated and untreated cell lines were compared.

The results (shown in Table 5 and Fig. 6) indicate that the scratch created by the untreated MCF-7 cells dramatically narrowed by 81.62 % after 48 h. However, compound **22** treatment on MCF-7 cells resulted in a 30.20 % reduction in scratch width, indicating that the compound **22** significantly supressed the growth of MCF-7 cells.

2.3. *Computational studies*

2.3.1. *Molecular docking*

Molecular docking experiments were executed utilizing the Molecular Operating Environment (MOE, 2019) software to find out the binding modes and energy scores of the obtained thiazolidine-2,4-dione compounds, **18**–**24**, with the ATP pocket of VEGFR-2. The X-ray crystallographic structure of the VEGFR-2 (PDB ID: 2OH4) was obtained from PDB. The co-crystallized ligand was docked again in the VEGFR-2 active site to validate the docking technique. The co-crystallized and docked ligands were overlaid with an RMSD of 0.84 Å, indicating the precision of the docking job (Fig. 7).

The synthetic thiazolidine-2,4-dione derivatives **18**–**24** exhibited a binding pattern that was largely similar to sorafenib's. Table 6 and Fig. 8 A-H displayed the energy scores and emphasized the binding patterns of the synthesized derivatives **18**–**24**. In line with the docking outcomes, all members had the same aptitude to ascertain the VEGFR-2 binding site and bond with its essential amino acids in a similar way to sorafenib. More specifically, the active site's hinge region was occupied by the 5-benzylidenethiazolidine-2,4-dione motif of compounds **18**–**24** made crucial bonding with the amino acid Cys917. Also, the phenylacetamide linker was also steered into the gatekeeper region, resulting in hydrophobic interactions with Val897, Val914, and Cys1043. The amide, diamide, and hydrazide groups of the synthesized candidates served as pharmacophore moieties and achieved two significant bonds with Glu883 and Asp1044

Table 3
In vitro cytotoxicity of compound **22** against Vero cells and its selectivity index against HepG2, and HCF-7 cell lines.

Compound	Vero IC_{50} (μM)[a]	Selectivity index	
		HepG2	MCF-7
22	3.97 ± 0.05	1.95	3.28

[a] The results are the mean of three experiments.

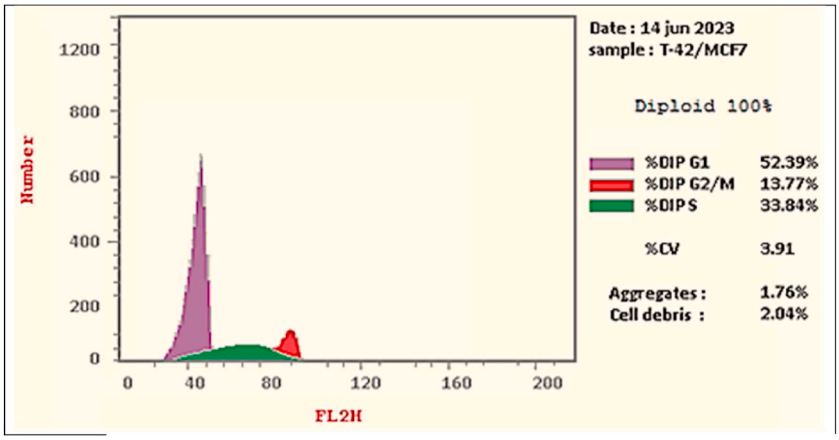

Fig. 4. Cell cycle analysis of MCF-7 cells treated with compound **22** at a concentration of 1.21 μM.

Table 4
Cell cycle analysis of **22**/MCF-7 at the concentration of 1.21 μM for 72 h.

Sample	Cell cycle distribution (%)[a]		
	G0-G1	S	G2/M
22 treated MCF-7 cells	52.39	33.84	13.77
Control MCF-7 cells	59.04	24.61	16.35

[a] Values are reported as mean of three different experiments.

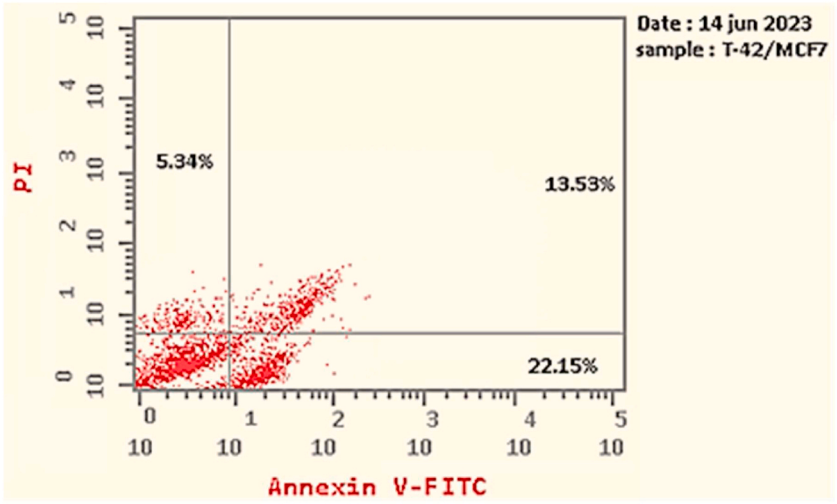

Fig. 5. Apoptosis analysis of MCF-7 cells treated with compound **22** at a concentration of 0.53 μM for 72 h.

Table 5
Effect of compound **22** on stages of the cell death process in MCF-7 cells after 72 h treatment.

Sample	Viable[a] (Left Bottom)	Apoptosis[a]		Necrosis[a] (Left Top)
		Early (Right Bottom)	Late (Right Top)	
Control MCF-7 cells	2.66	0.29	0.15	2.22
22 treated MCF-7 cells	41.02	22.15	13.53	5.34

[a] Values are reported as mean of three different experiments.

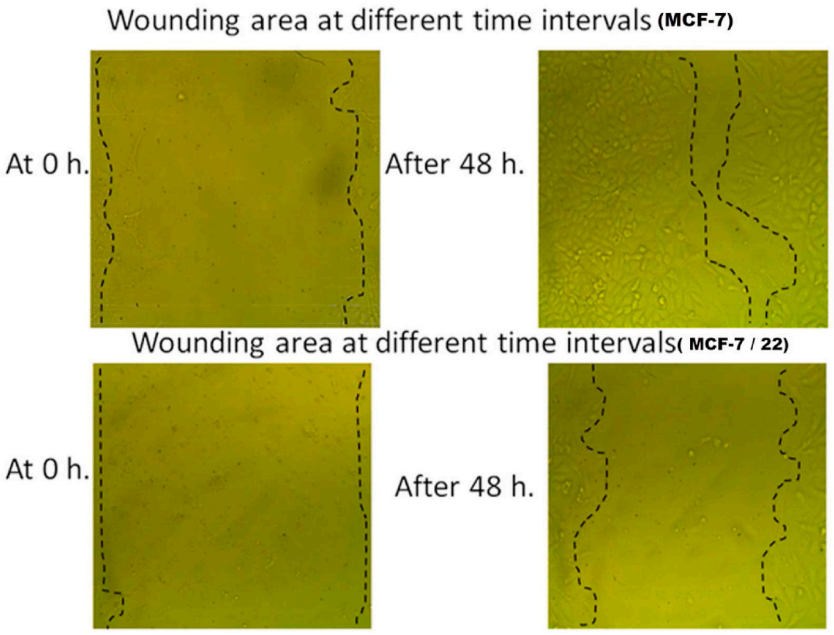

Fig. 6. The effect of compound **22** on MCF-7's migration and healing after 48 h.

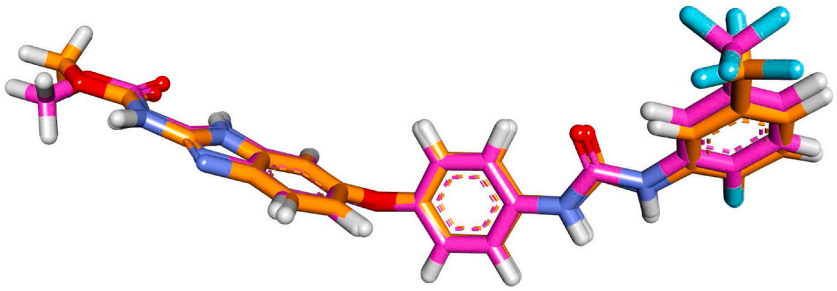

Fig. 7. Docked ligand (orange) superimposed on co-crystallized ligand (pink) in the VEGFR-2 active site. (For interpretation of the references to color in this figure legend, the reader is referred to the Web version of this article.)

Table 6
The effect of compound **22** on MCF-7's migration and healing after 48 h.

Item	at 0 h		at 24 h		at 48 h		RM um	Wound closure % um^2	Area difference %
	area	width	area	width	area	width			
Untreated MCF-7 cells	975.00	974.11	645.50	644.43	179.17	178.24	16.58	81.62	795.83
Treated MCF-7 cells with compound **22**	979.67	978.78	905.17	904.16	683.83	682.93	6.16	30.20	295.83

in the DFG motif region. Finally, the hydrophobic side chains of compounds **18**–**24** were able to interact with the hydrophobic side chains of the Ile886, Leu887, Ile890, Val896, Val897, Leu1017, and Ile1042 residues lining the back pocket of VEGFR-2, which allowed the compounds' hydrophobic substituents to achieve maximal fitting in the allosteric hydrophobic pocket in the active site.

2.3.2. In silico ADME analysis

The growing significance of predictive ADMET (absorption, distribution, metabolism, excretion, and toxicity) has been underscored in the field of medicinal chemistry and drug discovery [43]. Today, a diverse array of techniques, including high-throughput assay development and structure-based ADMET prediction, contribute to this field [44]. *In silico* ADMET studies help in identifying compounds with optimal pharmacokinetic properties, improving the chances of successful translation from preclinical to clinical stages [45]. Timely assessment of the ADMET properties of new compounds during early stages of drug development is paramount to

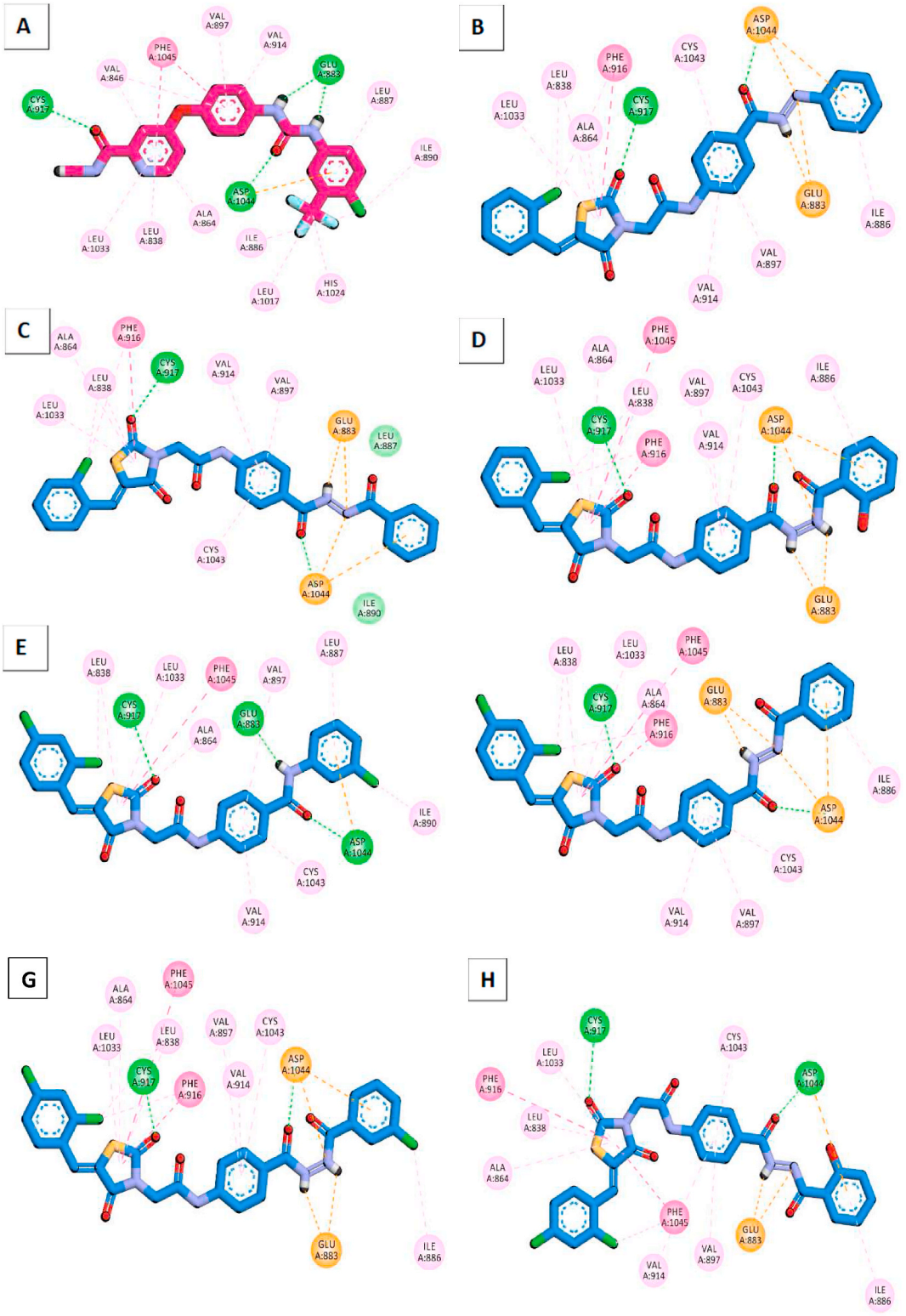

Fig. 8. Binding modes of sorafenib and the synthesized compounds against VEGFR-2. **A)** Sorafenib, **B)** derivative **18**, **C)** derivative **19**, **D)** derivative **20**, **E)** derivative **21**, **F)** derivative **22. G)** derivative **23. H)** derivative **24**.

prevent late as well as market withdrawal [46].

In this study, we employed computational methods utilizing Discovery Studio software to evaluate the ADMET profile of the synthesized thiazolidine-2,4-diones. Detailed findings are presented in Table 7 and Fig. 9. In general, the synthesized thiazolidine-2,4-diones displayed acceptable ranges within the ADMET profile. Notably, their projected negligible blood-brain barrier (BBB) penetration suggests potential safety concerning central nervous system (CNS) effects. Furthermore, the thiazolidine-2,4-diones were predicted to exert no inhibitory effects on CYP2D6, indicating anticipated liver safety. All compounds were expected to have poor human intestinal absorption levels. While, except for compounds **21** and **23** (showed very low aqueous solubility levels), the rest of thiazolidine-2,4-diones showed low aqueous solubility levels. Finally, it was anticipated that all compounds, except compound **20** would bind plasma proteins at quantities exceeding 90 %.

2.3.3. Toxicity studies

The utilization of in silico methods has become pivotal in the field of drug development due to their ability to minimize the reliance on time-consuming *in vitro* and *in vivo* experiments, resulting in reduced delays [47]. In this study, we employed the Discovery Studio software to evaluate the toxicity profile of the synthesized compounds. The results obtained from seven toxicity models, presented in Table 8 and a comprehensive data description was supplied in the **Supplemental Data (**Table 9**)**.

Remarkably, all the synthetic compounds exhibited a non-mutagenic and non-carcinogenic nature, as predicted by the Ames test and FDA carcinogenicity rodent models. Comparing sorafenib (14.244 mg/kg/day), the calculated carcinogenic potency TD_{50} values of the thiazolidine-2,4-diones ranged from 9.508 to 71.936 mg/kg/day. Moreover, all the thiazolidine-2,4-diones were predicted to possess oral LD_{50} values higher than sorafenib (0.823 g/kg), with a range of 1.378–3.625 g/kg. Furthermore, the calculated LOAEL values of the thiazolidine-2,4-diones, ranging from 0.011 to 0.035 g/kg, surpassed those of sorafenib (0.005 g/kg). Lastly, it was projected that the synthesized thiazolidine-2,4-diones would exhibit no dermal irritation (DI) and cause only mild ocular irritation (OI).

2.3.4. Molecular dynamic (MD) simulations

After roughly 50 ns, the RMSD for the apo protein (Fig. 10A: Blue Line) eventually stabilized at around 3.2 Å. The holo protein, on the other hand, displays a more or less consistent tendency throughout the simulation. It shows an average of 1.9 Å for the first 60 ns, then an increase in the values until it stabilizes at 2.8 Å over the final 50 ns (Fig. 10A: Red Line). According to the RMSF values, the difference between the two averages is attributable to the increased mobility of the Ile1042:Trp1069 loop in the apo protein compared to the holo protein (Fig. 10F). During the simulation, the RMSD of compound **22** (Fig. 10B) shows a consistent conformation beginning about 40 ns with an average of 4.5 Å. This high average is due to a change in the ligand's structure while in the binding pocket, as shown in the inset of Fig. 10B. According to Fig. 10C, the apo system and the holo system have RoG averages that are almost comparable with a difference of around 0.5 Å. Similarly, the average SASA values for apo and holo proteins vary by just around 500 $Å^2$ (Fig. 10D). According to Fig. 10E, the apo and holo systems have almost the same number of H-bonds on average (69 bonds). Overall, this seems to show that both proteins are stable and that neither undergoes any significant structural changes throughout the simulation. Furthermore, the oscillations of the C-alpha atoms in the Ile1042:Trp1069 loop between the RMSFs of the two systems varied by 5 Å, with the apo protein having the highest RMSF of 8 Å (Fig. 10F). The fact that compound **22** has a consistent average distance between the protein and ligand centers of mass (approximately 7.4 Å) indicates that the interaction is steady (Fig. 10G).

The different components of the binding free energy computed using the MM-GBSA approach was depicted in Fig. 11. The fact that compound **22** has a binding energy of −37.54 kcal/mol indicates that there is considerable interaction between the two entities. van der Waals contacts seem to be more important than electrostatic interactions in the process of establishing binding stability (−57.38 Kcal.mol^{-1}vs. −18.58 kcal mol^{-1}). We were able to identify the contributions produced by amino acids that are within 0.5 nm of compound **22** utilizing decomposition analysis (Fig. 12). The amino acids Leu838 (−1.56 kcal mol^{-1}), Val846 (−1.42 kcal mol^{-1}), Leu866 (−1.21 kcal mol^{-1}), Leu887 (−1.56 kcal mol^{-1}), Val897 (−1.29 kcal mol^{-1}), Val914 (1.17 kcal mol^{-1}), Leu1033 (−1.4 kcal mol^{-1}), Cys1043 (−2.75 kcal mol^{-1}), Phe1045 (−3.18 kcal mol^{-1}) and Arg1049 (−1.42 kcal mol^{-1}) are the ones that are within 0.5 nm and have a share of better than −1 kcal/mol.

According to the ProLIF library's results, 11 amino acids exhibit a higher than 94 % prevalence of hydrophobic interaction. The following amino acids interacted with compound **22** the most frequently: Leu838 (95.1 %), Val846 (99.2 %), Leu887 (97.2 %), Val897 (98.2 %), Val914 (99 %), Arg1030 (94.4 %), Leu1033 (94.3 %), Cys1043 (99.9 %), Asp1044 (98.7 %), Phe1045 (99.4 %) and Arg1049 (99.5 %) (Fig. 13 A-C). The PLIP webserver was used to detect and generate 3D binding interactions in the form of. pse files from

Table 7
Binding pattern and ΔG of the thiazolidine-2,4-diones **11a-g**.

Comp.	Binding score [Kcal/mol]	Number of hydrogen bonds	Number of hydrophobic bonds/Number of electrostatic interactions
Sorafenib	−21.02	4	16/1
18	−21.44	2	10/4
19	−21.15	2	9/4
20	−21.16	2	11/4
21	−22.10	3	10/1
22	−21.00	2	10/4
23	−21.47	2	11/4
24	−21.13	2	11/3

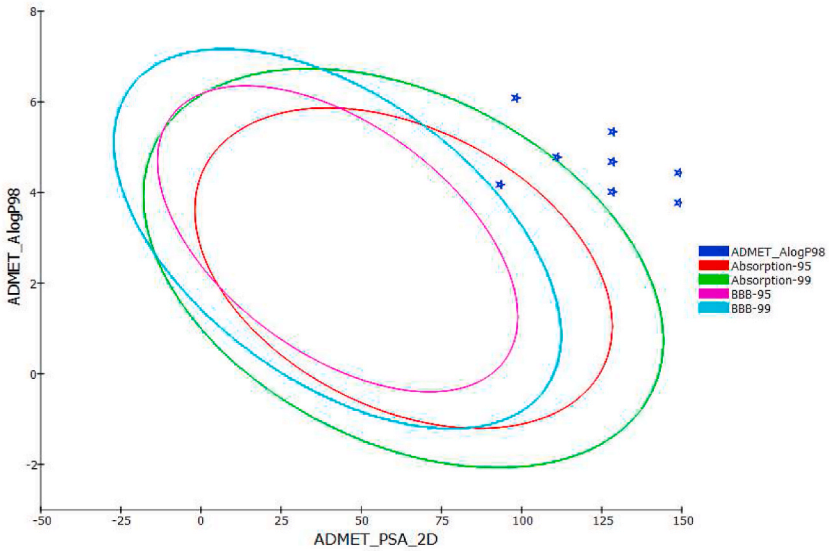

Fig. 9. ADMET descriptors of the synthesized thiazolidine-2,4-diones.

Table 8
ADMET screening of the synthesized thiazolidine-2,4-diones.

Comp.	BBB level	Solubility (aqueous) level	Absorption (human-intestine) level	CYP2D6 (Inhibition) prediction	PPB (Binding) prediction
18	Very low	Low	Poor	No inhibition	>90 %
19					
20					<90 %
21		Very low			>90 %
22		Low			
23		Very Low			
24		Low			
Sorafenib		Very low	Good		

Table 9
Toxicity study of the synthesized compounds.

Comp.	Ames prediction	Mouse- Female FDA	Carcinogenic Potency TD_{50} (Rat)[a]	RMT feed	Rat Oral LD_{50}[b]	Rat Chronic LOAEL[b]	DI	OI
18	Non-Mutagen	Non-Carcinogen	21.284	0.134	2.806	0.030	Non-Irritant	Mild Irritant
19			32.929	0.076	2.820	0.022		
20			71.936	0.249	3.625	0.035		
21			9.508	0.044	1.866	0.008		
22			29.544	0.060	1.378	0.020		
23			10.643	0.048	1.989	0.011		
24			64.428	0.197	1.769	0.032		
Sorafenib		Single-Carcinogen	14.244	0.089	0.823	0.005		

[a] Unit: mg/kg/day.
[b] Unit: g/kg.

representative frames created from clustering (Fig. 14).

PCA Was employed to determine the coordinated motions of the systems. The size of the reduced subspace was determined by the scree plot, the eigenvectors' distribution, and the cumulative sum (more details can be found in the methods section). The slope of the line seems to decline at the third PC of the scree plot. The first eigenvector alone accounted for around 64.2 % of the overall variance, whereas the sum of the 1st three eigenvectors accounted for approximately 74.7 % of the total variance (Fig. 15). The distribution of the first two PCs was found not to follow a Gaussian pattern (Fig. 16). In general, we determined that the top three eigenvectors best represented the reduced subspace.

The cosine content was calculated for the apo as well as holo VEGFR-2 to assess the level of randomness shown by the behavior of the 1st ten eigenvectors. Except for the third PC of the holo protein, which had a value of 0.3, the cosine content of the 1st ten

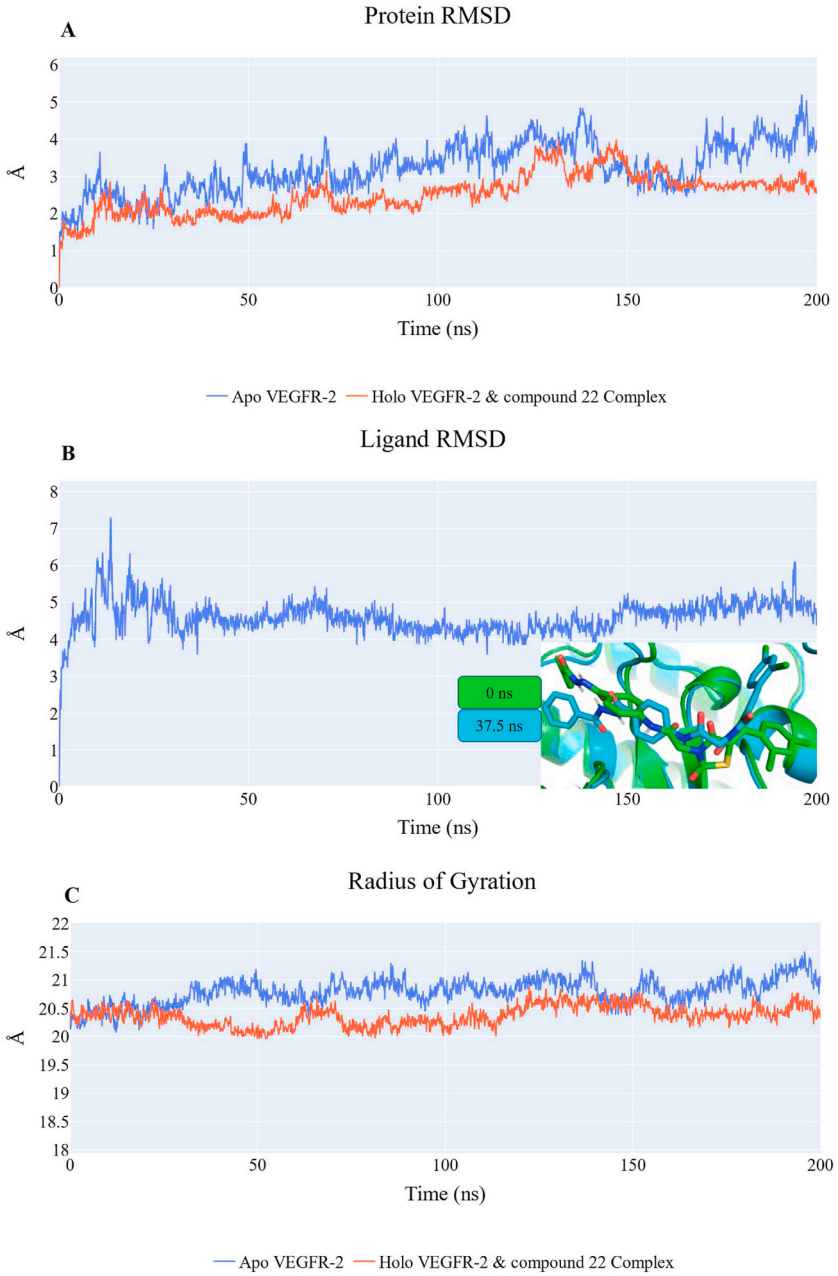

Fig. 10. MD simulation studies for VEGFR-2/compound **22** complex. **A**) RMSD values for the VEGFR-2 protein in apo (blue) and holo forms (red), B) shows the ligand RMSD values, **C**) radius of gyration for the VEGFR-2 protein in apo (blue) and holo forms (red), **D**) SASA for the VEGFR-2 protein in apo (blue) and holo forms (red), **E**) change in the number of hydrogen bonds for the VEGFR-2 protein in apo (blue) and holo forms (red l), **F**) RMSF for the VEGFR-2 protein in apo (blue) and holo forms (red), **G**) distance between the center of mass of compound **22** and the VEGFR-2. (For interpretation of the references to color in this figure legend, the reader is referred to the Web version of this article.)

eigenvectors in the apo and holo proteins was less than 0.2 (Fig. 17). The Root Mean Square Inner Product (RMSIP) displays an 8.2 % similarity between the two subspaces (the first three eigenvectors). This implies that there is a small similarity between the two subspaces. Furthermore, the RMSIP discovered that the C matrices of apo and holo proteins are only 19.2 % similar, indicating that the sampling differed between the two systems.

The results of projecting each trajectory onto the 1st three eigenvectors of the new C matrix are demonstrated in Figs. 18–20. The bigger marker in each of these graphs reflects the corresponding trajectory's average structure. Fig. 18, a projection on the first two eigenvectors, reveals that the two trajectories have separate average structures and that the frames reflect different sampling with just

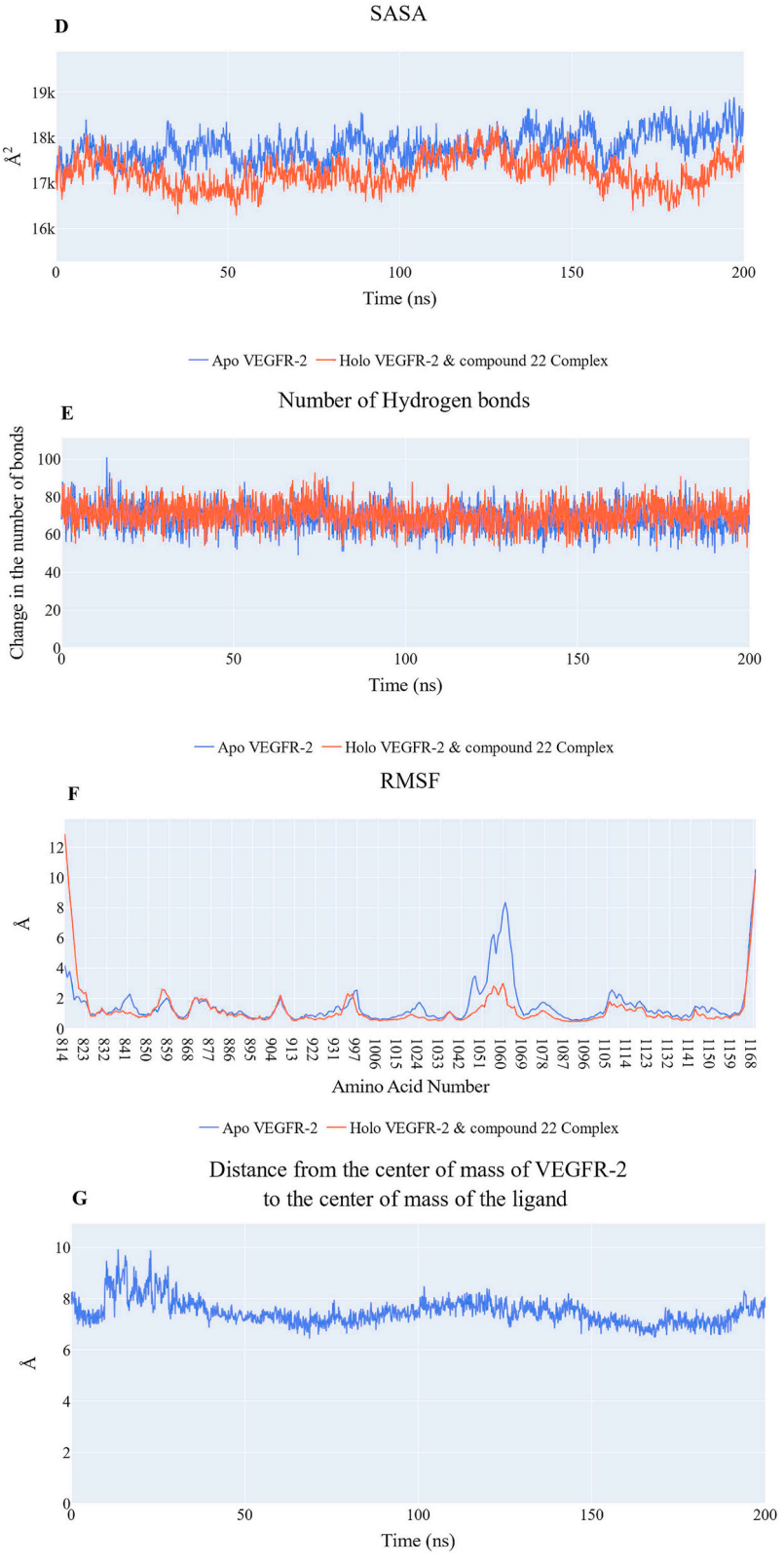

Fig. 10. (*continued*).

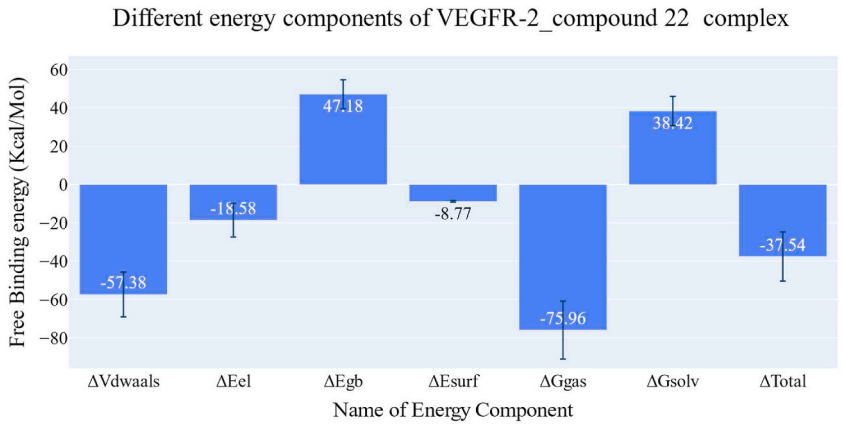

Fig. 11. Different energetic components of MM-GBSA and their values. Bars represent the standard deviations.

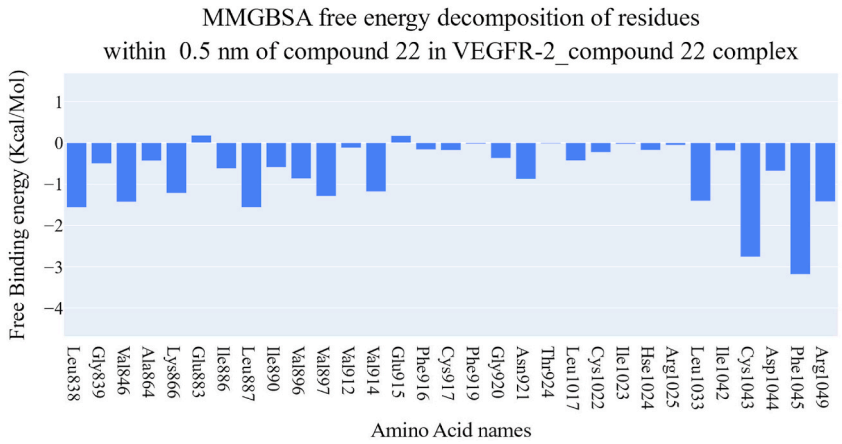

Fig. 12. Binding free energy decomposition of the VEGFR-2_22 complex.

a little degree of overlap at the start of the simulation (pale red and white dots). Furthermore, the sampling of the holo protein trajectory (represented by the red dots) in contrast to the apo protein demonstrates that the frames are more equivalent to one another for most of the time (clustered in one region). Fig. 19 (projection in the first and third PCs) shows that the two trajectories have a minor overlap and that their average structures are significantly different. Furthermore, the majority of the frames of the holo system, shown by the red dots, continued to exhibit a clustering tendency similar to that seen in Fig. 18. The apo protein, on the other hand, has significant variability among its frames. Similarly, the projection on the 2nd and 3rd eigenvectors, as shown in Fig. 20, indicates that they are distinct and have very little overlap in the early frames. The motion captured by the 1st three eigenvectors may be shown by porcupine diagrams, which were generated for this purpose (Fig. 21). The Asp1050:Pro1066 loop is shown to open in the first three PCs of both the apo protein (green structure), albeit in distinct orientations and magnitudes. The first PC of the holo trajectory (red structure) exhibits a clockwise twisting of the loop, while the second PC displays a closing motion. Similarly to the first PC, the third PC displays a clockwise twisting of the loop, but with a lesser magnitude.

2.3.5. DFT calculations

After drawing the structure of compound **22**, which contains 292 electrons and is composed of 56 atoms, the optimization process has been performed using Gaussian 09 software under DFT/B3LYP/6–311++G (d, p) theory level. The optimized chemical structure is labeled (Fig. 22a) and the Mulliken charge distribution function within compound **22**atoms has been carried out. The atomic charge distribution with color scale is presented in Fig. 22b, where the hydrogen atoms have a positive charge, all oxygens have a negative charge, and the most positive charges of carbon are concentrated on C19 and C31. All nitrogen atoms acquired negative charge except for N25, while the most negative carbons are focused on C7 and C33. Such findings conclude that the prepared drug has a significant charge delocalization which qualifies the molecule to bind with the target as the positively charged atoms of compound **22** could be attacked by nucleophilic centers of the target while the negatively charged atoms of compound **22** could be attacked by electrophilic centers of the target.

The theoretical dipole moment (Dm) and total ground energy (TE) are calculated and listed in Table 10. The chemical reactivity of

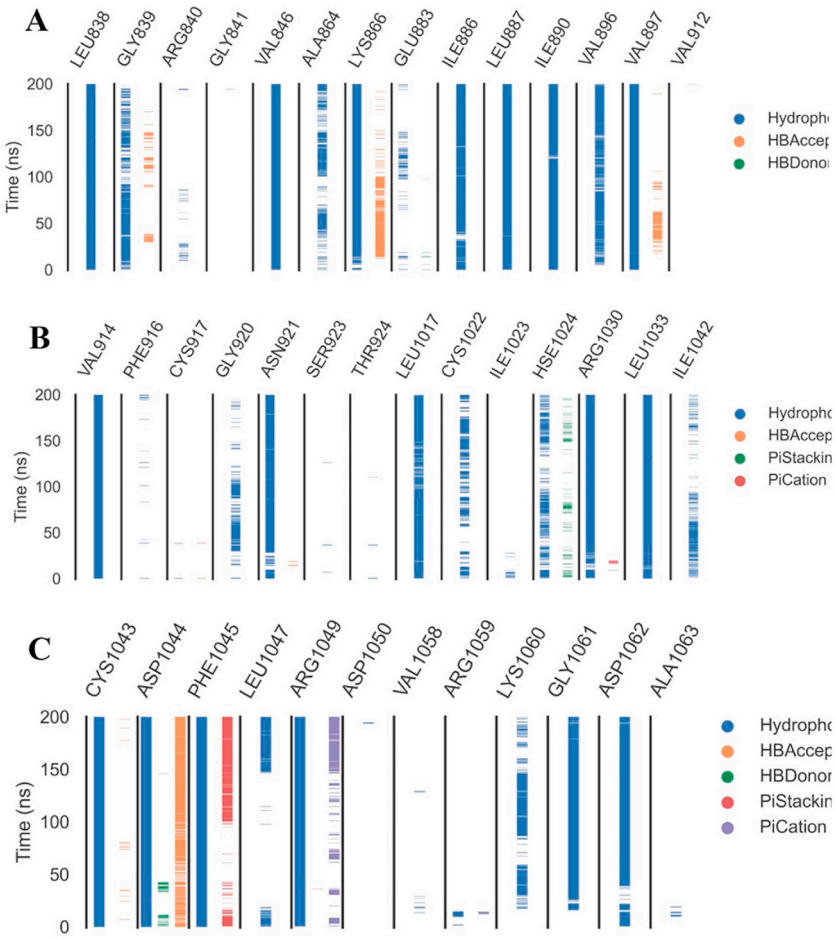

Fig. 13. Names of amino acids, types of interactions with compound **22**, and their occurrence during the whole simulation time using the ProLIF Python library.

the synthesized drug is strongly related to the energy gap, E_g, between HOMO and LUMO (the frontiers molecular orbitals; FMO) and global reactivity indices that are based on the HOMO and LUMO energies [48].

The analysis of FMO is displayed in Fig. 22c, both LUMO and HOMO functions are localized over dichlorobenzylidene dioxothizolidin acetaldehyde moiety and the energy gap between both orbitals are small of 3.054 eV, suggesting the ease of HOMO-LUMO electronic transition. The quantum parameters related to the energies of HOMO and LUMO are determined and tabulated in Table 10. The results conducted that compound **22**is biologically active with a high softness value [49].

To determine the electrophilic, nucleophilic and hydrophobic interaction centers within the geometry and understand the behavior of binding with the target, molecular electrostatic potential (ESP) is estimated, Fig. 22d. The ESP surface map showed that the positive ESP (deficient in electrons) is localized over hydrogens (blue batches), while the negative ESP is localized over oxygen atoms and colored red. The negative ESP zones are rich in electrons and act as hydrogen bonding acceptors, while the ESP green zones are responsible for hydrophobic interactions.

The spectrum of the total density of electrons (TDOS) was analyzed using GaussSum software and results were conducted that orbitals under HOMO include the highest TDOS, as seen in Fig. 22e.

To indicate the interactions between the atoms in the prepared drug, the quantum theory of atoms in molecules (QTAIM) has been analyzed using Multiwfn and AIMALL programs after getting the optimized log file. Such topological analysis has been performed in terms of bond paths and bond critical points and the quantum functions; electron density (ρ), Laplacian ($\nabla^2\rho$), and energy density H(r) values have been estimated and listed in Supplementary Data (Table S1 and Fig. S3). The geometrical graph in Fig. 22f shows that the three folded compound has generated three new bond paths, Fig. 22g. The QTAIM function (ρ) > 0.1 au while ($\nabla^2\rho$)>0 suggests a non-covalent (closed-shell) bonding. Also, the total energy density (H(r)) > 0, suggesting bonding of electrostatic nature. Such findings enhance the geometrical stability of compound **22**.

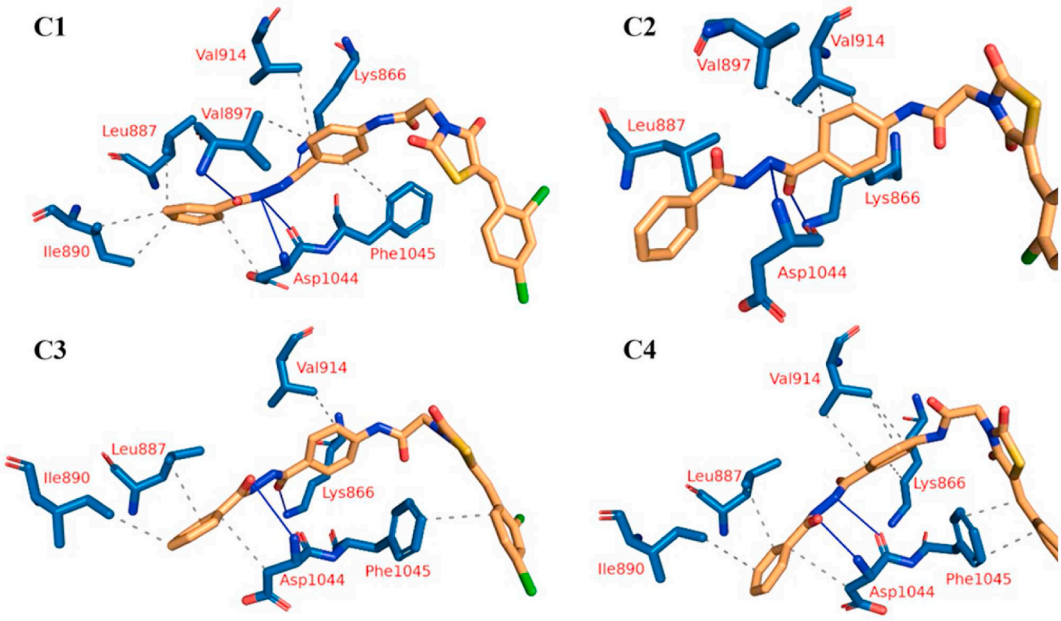

Fig. 14. Five representative clusters obtained from TTClust and their 3D interactions with molecule **22**. Grey dashed lines: hydrophobic interactions, blue solid lines: H-bonds, orange sticks: compound **22**, blue sticks: amino acids of VEGFR-2 protein. (For interpretation of the references to color in this figure legend, the reader is referred to the Web version of this article.)

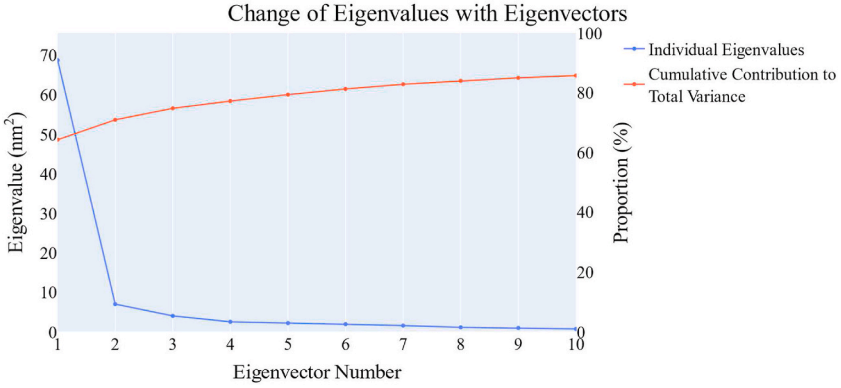

Fig. 15. Change in the eigenvalues with increasing the eigenvectors (blue line). The cumulative variance retained in the eigenvectors (red line). (For interpretation of the references to color in this figure legend, the reader is referred to the Web version of this article.)

3. Conclusion

Our study successfully designed and synthesized seven novel 2,4-dioxothiazolidine derivatives with promising anticancer and VEGFR-2 inhibiting capabilities. SAR study revealed that the positive effect of the pharmacophore moieties on VEGFR-2 inhibitory activities can be arranged descendingly as amide > diamide > hydrazide. In addition, substituted phenyl ring (hydrophobic tail) with electron donating group is more advantageous than the substituted phenyl ring with electron withdrawing group. Compound **22** demonstrated the highest efficacy in inhibiting VEGFR-2 and exhibited significant anti-proliferative activity against HepG2 and MCF-7 cancer cell lines. Furthermore, compound **22** increased the apoptotic rate in MCF-7 cells with cell cycle arrest at S phase. Computational studies, including molecular docking, MD simulations, PLIP, and ED provided deep insights into the molecular, structural and energetic characteristics of the VEGFR-2-**22** complex. The study also indicated that compound **22** and other proposed compounds exhibited drug-like properties based on computational ADMET and toxicity experiments. Overall, our findings support the potential of compound **22** as an effective anticancer lead compound and highlight its utility as a model for future structural modifications and biological investigations.

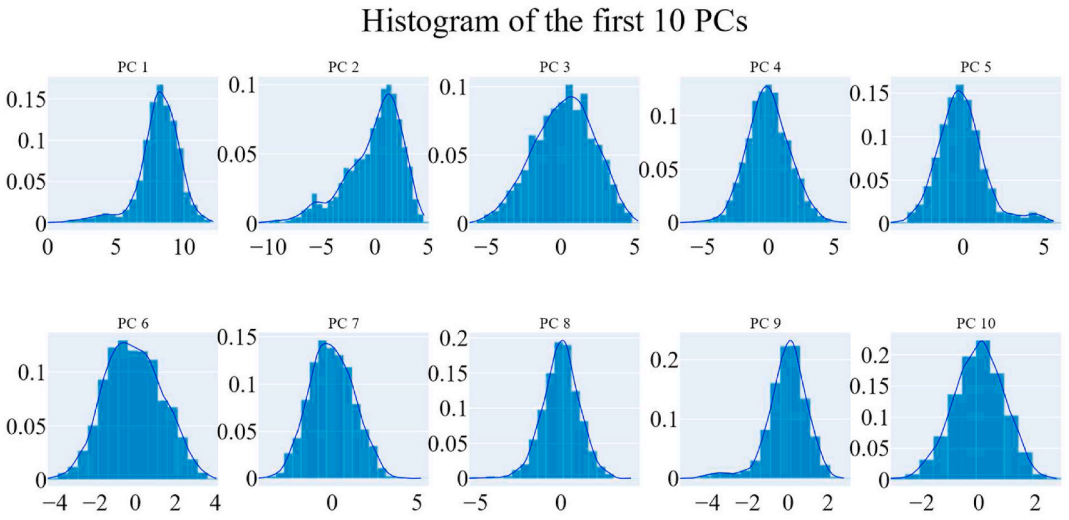

Fig. 16. The distribution of the first ten eigenvectors.

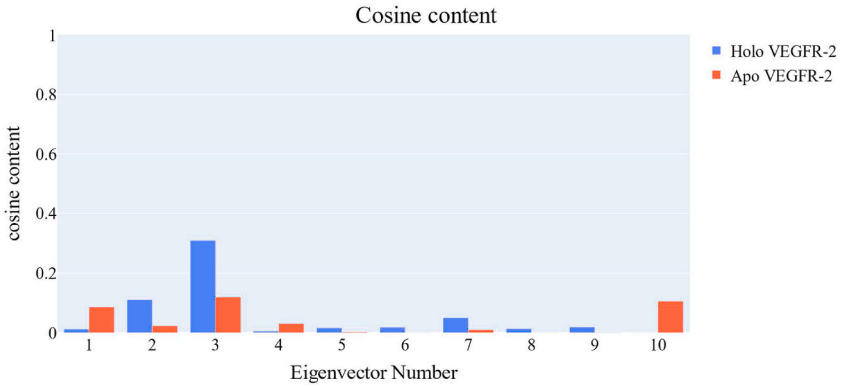

Fig. 17. Values of the cosine content of the 1st ten eigenvectors for the holo and the apo trajectories.

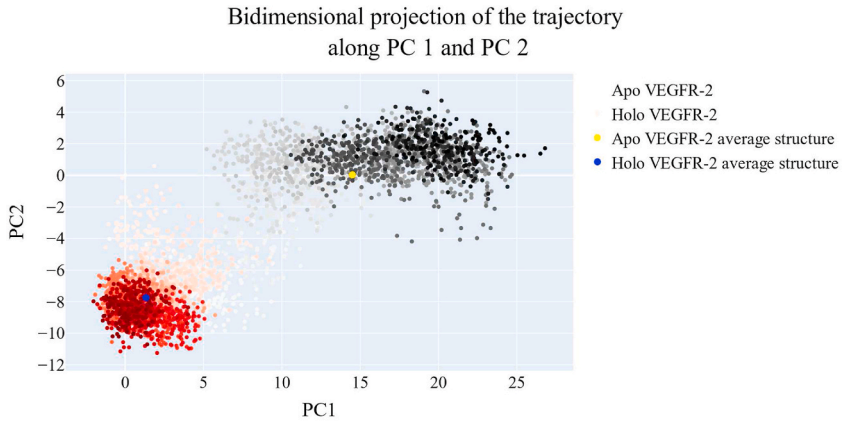

Fig. 18. Projection of each trajectory on the 1st two eigenvectors.

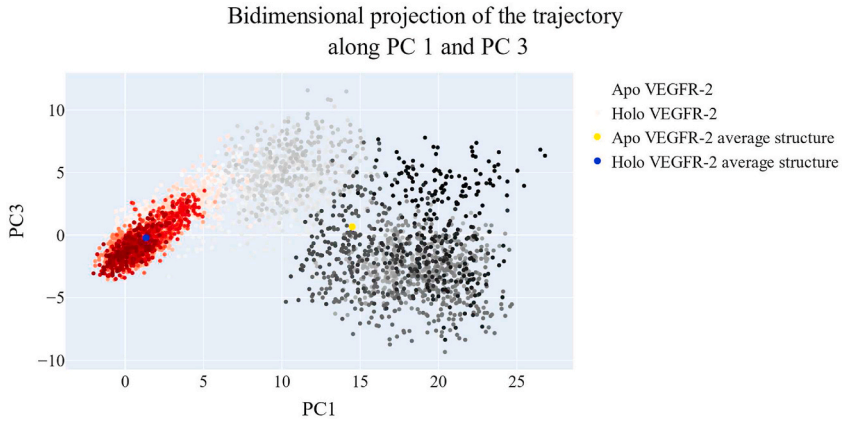

Fig. 19. Projection of each trajectory on the 1st and 3rd eigenvectors.

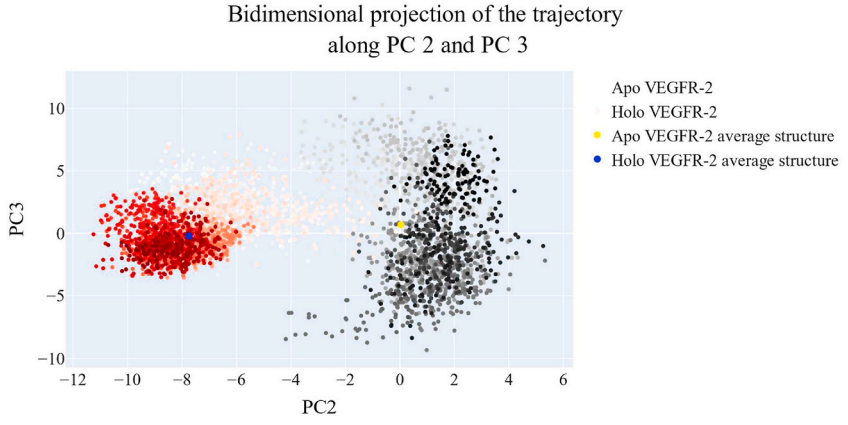

Fig. 20. Projection of each trajectory on the 2nd and 3rd eigenvectors.

4. Experimental

4.1. Chemistry

All the reagents, chemicals, apparatus were described in **Supplementary Data**. Compounds **3**, **5a,b**, **6a,b, 8, 9**, **11**, **13**, **15a-c**, **16a-c**, and **17a-c** were previously prepared [3,50–56].

4.1.1. The synthesis of compounds 18-24

Equimolar appropriate potassium salts **6a, b** (0.001 mol) were refluxed for 6 h with appropriate intermediates **11**, **13**, and/or **17a-c** (0.001 mol) in dry 10 mL of DMF and KI (catalytic amount). The reaction mixtures were poured onto 200 mL of ice water with constant stirring. The solid product formed was filtered, washed with water, and dried to give the target compounds **18**–**24**.

4.1.1.1. 2-(5-(2-Chlorobenzylidene)-2,4-dioxothiazolidin-3-yl)-N-(4-(2-phenylhydrazine-1-carbonyl)phenyl)acetamide 18. Off white crystal (yield, 65 %); m. p. = 235–237 °C; IR (KBr) ν cm^{-1}: 3268 (NH), 1745, 1694, 1667 (C═O); ^{1}H NMR (400 MHz, DMSO-d_6) δ ppm: 10.97 (s, 1H, NH), 10.89 (s, 1H, NH), 10.31 (s, 1H, NH), 8.11 (s, 1H, –C═CH), 7.94 (d, J = 7.6 Hz, 2H, Ar–H), 7.87 (s, 1H, Ar–H), 7.73 (d, J = 9.2 Hz, 2H, Ar–H), 7.67 (d, J = 8.0 Hz, 2H, Ar–H), 7.57–7.55 (s, 2H, Ar–H), 7.16 (m, 1H, Ar–H), 6.81 (d, J = 7.6 Hz, 2H, Ar–H), 6.72 (m, 1H, Ar–H), 4.61 (s, 2H, CH_2); ^{13}C NMR (101 MHz, DMSO-d_6) δ ppm: 167.36, 166.25, 165.39, 164.67, 150.07, 135.01, 132.72, 131.35, 130.91, 130.86, 129.55, 129.30, 129.19, 128.84, 128.71, 128.46, 128.22, 125.21, 119.16, 119.06, 112.82, 44.74; Mass (m/z): 508 (M^+ + 2, 23.56 %), 506 (M^+, 8.02 %), 97 (100 %, base peak); $C_{25}H_{19}ClN_4O_4S$ (506.96).

4.1.1.2. 4.1.N-(4-(2-(3-chlorobenzoyl)hydrazine-1-carbonyl)phenyl)-2-(5-(2-chlorobenzyl idene)-2,4dioxothiazolidin-3-yl)acetamide 19. White crystal (yield, 72 %); m. p. = 221–223 °C; IR (KBr) ν cm^{-1}: 3268 (NH), 1745, 1694, 1667 (C═O); ^{1}H NMR (400 MHz, DMSO-d_6) δ ppm: 10.77 (s, 1H), 10.58 (s, 2H), 8.11 (s, 1H), 7.97–7.89 (m, 6H), 7.73 (m, 2H), 7.65 (m, 2H), 7.567.53 (m, 2H), 4.63 (s, 2H); ^{13}C NMR (101 MHz, DMSO-d_6) δ ppm: 167.36, 165.71, 165.38, 165.02, 164.73, 142.00, 135.04, 133.87, 132.69, 132.20, 131.31, 131.05,

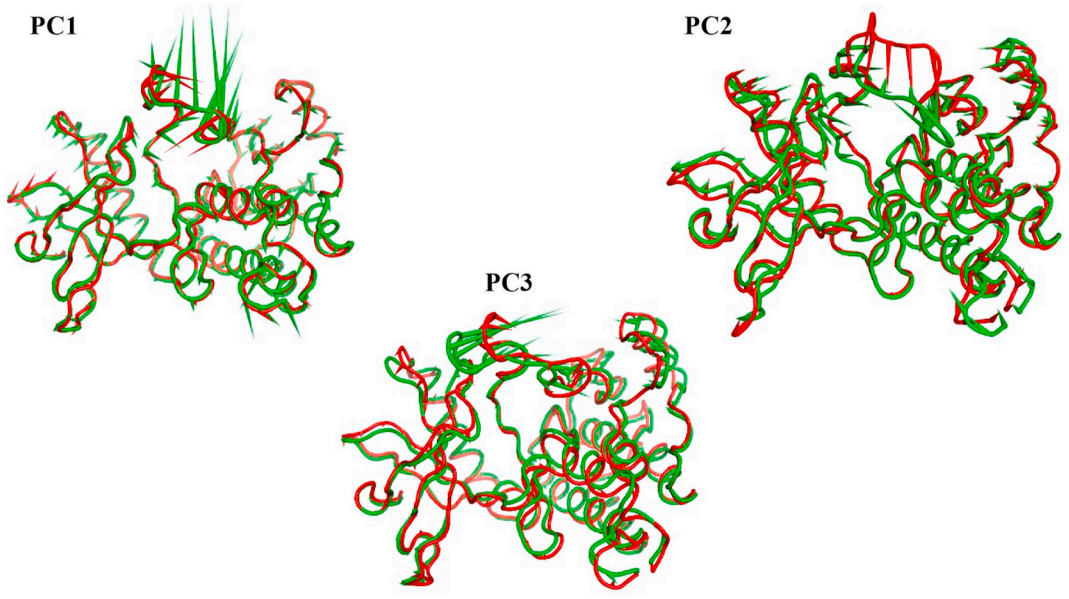

Fig. 21. Porcupine representations of each of the 1st three eigenvectors for apo(green) and holo (red) cartoon protein trajectories. (For interpretation of the references to color in this figure legend, the reader is referred to the Web version of this article.)

130.88, 129.51, 129.32, 129.09, 128.66, 127.87, 127.76, 126.66, 125.13, 119.10, 44.74; Mass (*m/z*):569 (M^+, 18.80 %), 390 (100 %, base peak); $C_{26}H_{18}Cl_2N_4O_5S$ (569.41).

4.1.1.3. 2-(5-(2-Chlorobenzylidene)-2,4-dioxothiazolidin-3-yl)-N-(4-(2-(2-hydroxybenzoyl) hydrazine-1-carbonyl)phenyl)acetamide 20. White crystal (yield, 70 %); m. p. = 228–230 °C; IR (KBr) ν cm^{-1}: 3566 (OH), 3267 (NH), 1745, 1694, 1668 (C═O); ^{1}H NMR (400 MHz, DMSO-d_6) δ ppm: 11.93 (s, 1H, OH), 10.75 (s, 2H, 2NH), 10.63 (s, 1H, NH), 8.12 (s, 1H, –C═CH), 7.94 (d, J = 6.4 Hz, 2H, Ar–H), 7.87 (s, 1H, Ar–H), 7.73 (d, J = 6.6 Hz, 2H, Ar–H), 7.67 (d, J = 8.0 Hz, 2H, Ar–H), 7.57–7.55 (m, 2H, Ar–H), 7.47 (s, 1H, Ar–H), 6.99 (m, 2H, Ar–H), 4.62 (s, 2H, CH_2); ^{13}C NMR (101 MHz, DMSO-d_6) δ ppm: 168.25, 167.36, 165.48, 165.39, 164.74, 159.81, 142.03, 135.04, 134.63, 132.69, 131.34, 130.89, 129.53, 129.34, 129.13, 128.79, 128.66, 127.76, 125.16, 119.51, 119.13, 117.89, 115.07, 44.75; Mass (*m/z*): 551 (M^+ +1, 18.31 %), 550 (M^+, 65.70 %), 369 (100 %, base peak); $C_{26}H_{19}ClN_4O_6S$ (550.97).

4.1.1.4. N-(3-chlorophenyl)-4-(2-(5-(2,4-dichlorobenzylidene)-2,4-dioxothiazolidin-3-yl) acetamido)benzamide 21. Off white crystal (yield, 78 %); m. p. = 208–210 °C; IR (KBr) ν cm^{-1}: 3265 (NH), 1745, 1693, 1667 (C═O); ^{1}H NMR (400 MHz, DMSO-d_6) δ ppm: 10.79 (s, 1H, NH), 10.32 (s, 1H, NH), 8.03 (s, 1H, –C═CH), 7.98 (m, 3H, Ar–H), 7.86 (s, 1H, Ar–H), 7.73 (d, J = 6.0 Hz, 3H, Ar–H), 7.64 (s, 2H, Ar–H), 7.39 (d, J = 7.3 Hz, 1H, Ar–H), 7.15 (d, J = 6.8 Hz, 1H, Ar–H), 4.61 (s, 2H, CH_2); ^{13}C NMR (101 MHz, DMSO-d_6) δ ppm: 167.13, 165.49, 165.29, 164.68, 141.96, 141.23, 136.40, 135.95, 133.40, 130.74, 130.67, 130.49, 130.38, 129.82, 129.35, 128.91, 128.20, 125.76, 123.66, 120.15, 119.06, 118.99, 44.77; Mass (*m/z*): 560 (M^+, 43.15 %), 198 (516 %, base peak); $C_{25}H_{16}Cl_3N_3O_4S$ (560.83).

4.1.1.5. N-(4-(2-benzoylhydrazine-1-carbonyl)phenyl)-2-(5-(2,4-dichlorobenzylidene)-2,4-dioxothiazolidin-3-yl)acetamide 22. White crystal (yield, 74 %); m. p. = 220–222 °C; IR (KBr) ν cm^{-1}: 3263 (NH), 1745, 1694, 1666 (C═O); ^{1}H NMR (400 MHz, DMSO-d_6) δ ppm: 10.73 (s, 1H, NH), 10.48 (s, 1H, NH), 10.44 (s, 1H, NH), 8.04 (s, 1H, –C═CH), 7.94 (d, J = 5.6 Hz, 4H, Ar–H), 7.86 (s, 1H, Ar–H), 7.71 (d, J = 6.7 Hz, 2H, Ar–H), 7.65 (s, 2H, Ar–H), 7.60 (m, 1H, Ar–H), 7.55–7.53 (m, 2H, Ar–H), 4.61 (s, 2H, CH_2); ^{13}C NMR (101 MHz, DMSO-d_6) δ ppm: 167.12, 166.36, 165.74, 165.29, 164.67, 141.91, 136.41, 135.96, 133.09, 132.32, 130.67, 130.49, 130.38, 129.06, 128.98, 128.92, 128.19, 128.04, 127.94, 125.76, 119.08, 44.78; Mass (*m/z*): 569 (M^+, 34.38 %), 529 (100 %, base peak); $C_{26}H_{18}Cl_2N_4O_5S$ (569.41).

4.1.1.6. N-(4-(2-(3-chlorobenzoyl)hydrazine-1-carbonyl)phenyl)-2-(5-(2,4-dichloro benzylidene)-2,4-dioxothiazolidin-3-yl)acetamide 23. White crystal (yield, 80 %); m. p. = 217–219 °C; IR (KBr) ν cm^{-1}: 3267 (NH), 1745, 1694, 1667 (C═O); ^{1}H NMR (400 MHz, DMSO-d_6) δ ppm: 10.75 (s, 1H, NH), 10.64 (s, 1H, NH), 10.52 (s, 1H, NH), 8.03 (s, 1H, –C═CH), 7.97–7.91 (m, 6H, Ar–H), 7.81 (s, 1H, Ar–H), 7.74–7.72 (m, 2H, Ar–H), 7.62 (m, 2H, Ar–H), 4.62 (s, 2H, CH_2); ^{13}C NMR (101 MHz, DMSO-d_6) δ ppm: 167.10, 165.72, 165.28, 165.03, 164.66, 141.99, 136.42, 135.98, 135.01, 133.88, 132.19, 131.03, 130.62, 130.45, 130.32, 129.09, 128.86, 128.16, 127.90, 127.77, 126.66, 125.68, 119.11, 44.78; $C_{26}H_{17}Cl_3N_4O_5S$ (603.86).

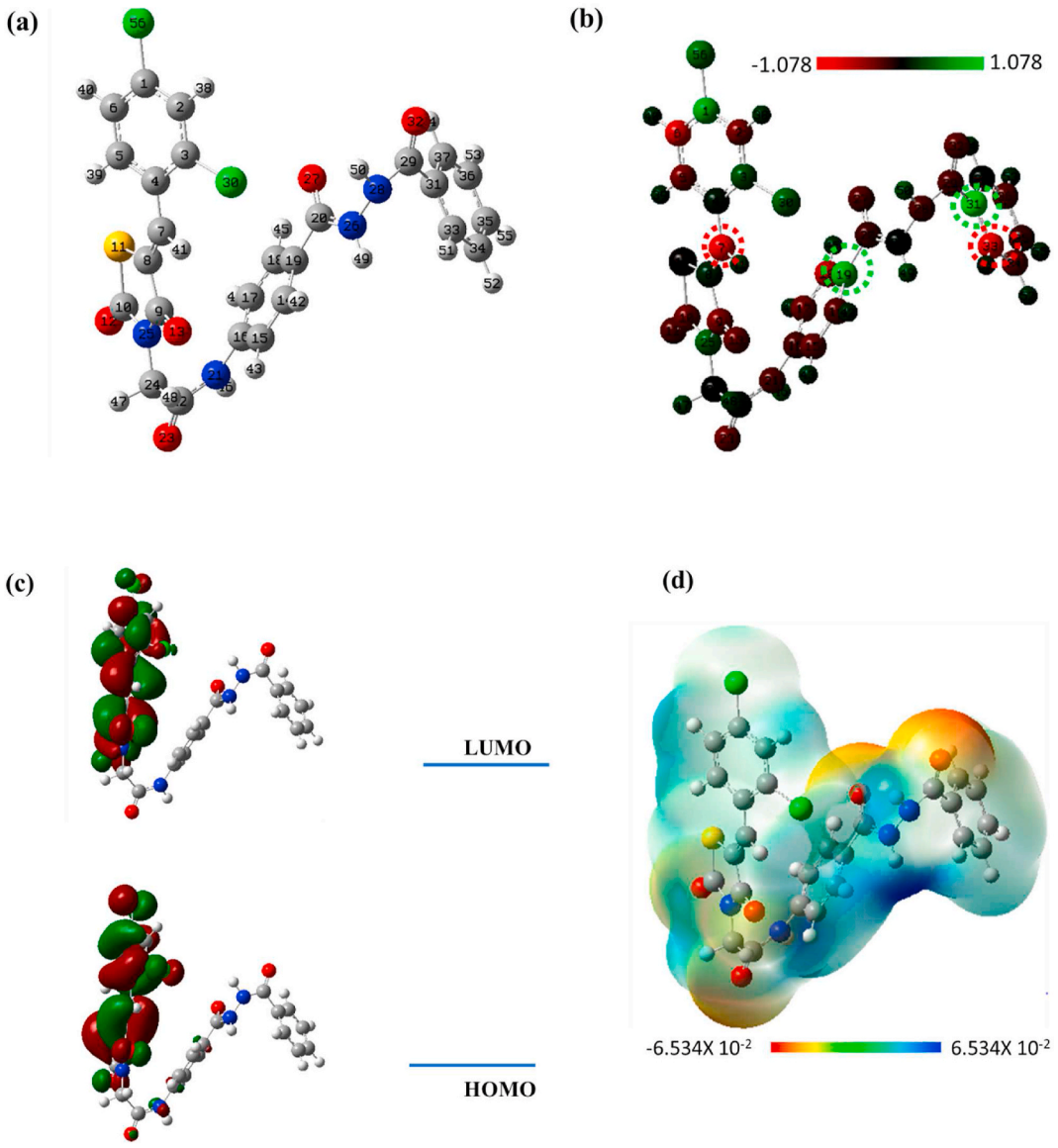

Fig. 22. The optimized geometry (a), the Mullikan atomic charge distribution (b), the FMO (c), the ESP (d), the TDOS (e), and the QTAIM maps (f and g) at B3LYB/6–311++G(d,p) for compound **22**.

4.1.1.7. 2-(5-(2,4-Dichlorobenzylidene)-2,4-dioxothiazolidin-3-yl)-N-(4-(2-(2-hydroxybenzoyl) hydrazine-1-carbonyl)phenyl)acetamide 24. White crystal (yield, 76 %); m. p. = 217–219 °C; IR (KBr) ν cm^{-1}: 3268 (NH), 1745, 1693, 1666 (C═O); ^{1}H NMR (400 MHz, DMSO-d_6) δ ppm: 11.90 (s, 1H, OH), 10.75 (s, 2H, 2NH), 10.62 (s, 1H, NH), 8.04 (s, 1H, –C═CH), 7.95–7.94 (m, 3H, Ar–H), 7.86 (s, 1H, Ar–H), 7.73 (d, J = 8.1 Hz, 2H, Ar–H), 7.65 (s, 2H, Ar–H), 7.47 (s, 1H, Ar–H), 6.98 (s, 2H, Ar–H), 4.62 (s, 2H, CH_2); ^{13}C NMR (101 MHz, DMSO-d_6) δ ppm: 168.25, 167.13, 165.45, 165.29, 164.69, 159.79, 142.02, 136.41, 135.96, 134.64, 130.67, 130.49, 130.37, 129.13, 128.91, 128.78, 128.20, 127.74, 125.75, 119.53, 119.10, 117.88, 115.04, 44.78; $C_{26}H_{18}Cl_2N_4O_6S$ (585.41).

4.2. Biological examinations

4.2.1. In vitro anti-proliferative activity

In vitro anti-proliferative activities of the target compounds were evaluated against HepG2 and MCF-7 cell lines *via* MTT assay [57–59] as described in **Supplementary Data**.

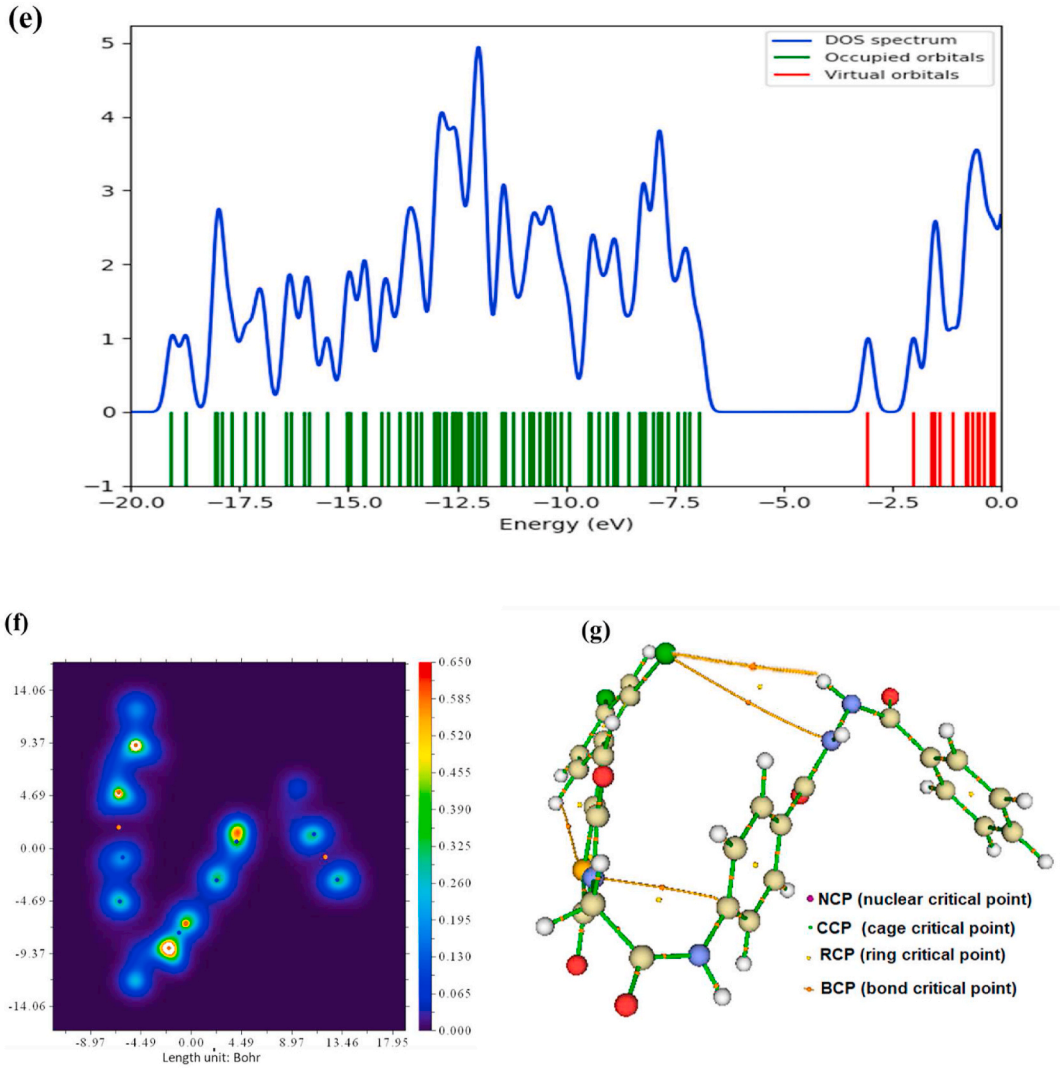

Fig. 22. (*continued*).

Table 10
The DFT global reactivity parameters for compound **22**.

IP	EA	μ (eV)	χ (eV)	η (eV)	σ (eV)	ω (eV)	Dm (Debye)	TE (eV)	ΔN_{max}	ΔE (eV)
6.920	−3.054	−1.933	1.933	4.987	0.201	9.321	1.490	−79344.7	0.388	−9.321

4.2.2. *In vitro VEGFR-2 inhibition*

VEGFR-2 inhibitory activities of the target compounds were evaluated using VEGFR-2 ELISA kit [60] as described in **Supplementary Data**.

4.2.3. *Cell cycle and apoptosis analysis*

The effect of compound **22** on apoptosis and cell cycle of MCF-7 was assessed according to the reported method shown in **Supplementary Data** [61–63].

4.2.4. *Cell migration assay*

Effect of compound **22** on cell migration apoptosis was assessed according to the reported method shown in **Supplementary Data** [64].

4.3. In silico studies

4.3.1. Docking studies

Binding modes and docking scores of the synthesized compounds against the crystal structure of VEGFR-2 [PDB ID: 2OH4, resolution: 2.05] were examined using MOE2019 as shown in **Supplementary Data** [65,66].

4.3.2. ADMET and toxicity studies

In silico ADMET and toxicity studies were performed using Discovery Studio 4.0 as shown in **Supplementary Data** [67–71].

4.3.3. MD simulations

CHARMM-GUI web server [72,73] and GROMACS 2021 [74,75] were used to carry out the MD simulations studies of compound **22**_VEGFR-2 complex as shown in **Supplementary Data.**

4.3.4. MM-GBSA and ProLIF analysis

Gmx_MMPBSA package [76,77] was used to test the MM-GBSA of compound **22**_VEGFR-2 complex as shown in **Supplementary Data** [78–80].

4.3.5. Essential dynamics cosine content, and bi-dimensional projections analysis

Essential Dynamics, cosine content, and bi-dimensional projections analysis of compound **22**_VEGFR-2 complex were evaluated by GROMACS [81–84] as shown in **Supplementary Data.**

4.3.6. DFT analyses

Gaussian software was used to carry out the DFT analyses of compound **22** as shown in **Supplementary Data** [73,85].

Data availability statement

All data regarding the presented work are available in the manuscript as well as in the supplementary materials.

CRediT authorship contribution statement

Ibrahim Eissa: Writing – original draft, Supervision, Project administration, Conceptualization. **Hazem Elkady:** Writing – original draft, Visualization, Validation, Software, Methodology, Data curation. **Mahmoud Rashed:** Writing – review & editing, Validation, Methodology. **Alaa Elwan:** Methodology, Investigation, Formal analysis. **Mohamed Hagras:** Validation, Resources, Methodology. **Mohammed A. Dahab:** Methodology. **Mohammed S. Taghour:** Methodology, Investigation. **Ibrahim M. Ibrahim:** Visualization, Validation, Software, Methodology, Investigation. **Dalal Z. Husein:** Visualization, Validation, Software, Methodology, Investigation. **Eslam B. Elkaeed:** Writing – review & editing, Funding acquisition. **Hanan A. Al-ghulikah:** Writing – review & editing, Funding acquisition. **Ahmed M. Metwaly:** Writing – review & editing, Writing – original draft, Supervision, Data curation. **Hazem A. Mahdy:** Writing – review & editing, Writing – original draft, Validation, Methodology.

Declaration of competing interest

The authors declare that they have no known competing financial interests or personal relationships that could have appeared to influence the work reported in this paper.

Acknowledgements

This research was funded by Princess Nourah bint Abdulrahman University Researchers Supporting Project number (PNURSP2024R95), Princess Nourah bint Abdulrahman University, Riyadh, Saudi Arabia. The authors extend their appreciation to the Research Center at AlMaarefa University for funding this work.

Appendix A. Supplementary data

Supplementary data to this article can be found online at https://doi.org/10.1016/j.heliyon.2024.e24005.

References

[1] R.L. Siegel, et al., Cancer statistics, 2021, Ca-Cancer J. Clin. 71 (1) (2021) 7–33.
[2] H.A. Al-Ghulikah, et al., New pyrimidine-5-carbonitriles as COX-2 inhibitors: design, synthesis, anticancer screening, molecular docking, and in silico ADME profile studies, Molecules 27 (21) (2022) 7485.

[3] N.A. Alsaif, et al., New quinoxaline derivatives as VEGFR-2 inhibitors with anticancer and apoptotic activity: design, molecular modeling, and synthesis, Bioorg. Chem. 110 (2021) 104807.
[4] C. Ma, et al., Design and synthesis of new quinoxaline derivatives as potential histone deacetylase inhibitors targeting hepatocellular carcinoma: in silico, in vitro, and SAR studies, Front. Chem. 9 (2021) 725135.
[5] M.M. Khalifa, et al., Topo II inhibition and DNA intercalation by new phthalazine-based derivatives as potent anticancer agents: design, synthesis, anti-proliferative, docking, and in vivo studies, J. Enzym. Inhib. Med. Chem. 37 (1) (2022) 299–314.
[6] R.G. Yousef, et al., New quinoxaline-2 (1 H)-ones as potential VEGFR-2 inhibitors: design, synthesis, molecular docking, ADMET profile and anti-proliferative evaluations, New J. Chem. 45 (36) (2021) 16949–16964.
[7] S.J. Modi, V.M. Kulkarni, Vascular endothelial growth factor receptor (VEGFR-2)/KDR inhibitors: medicinal chemistry perspective, Med. Drug Discov. 2 (2019) 100009.
[8] S.J. Modi, V.M. Kulkarni, Discovery of VEGFR-2 inhibitors exerting significant anticancer activity against CD44+ and CD133+ cancer stem cells (CSCs): reversal of TGF-β induced epithelial-mesenchymal transition (EMT) in hepatocellular carcinoma, Eur. J. Med. Chem. 207 (2020) 112851.
[9] E.B. Elkaeed, et al., In silico, in vitro VEGFR-2 inhibition, and anticancer activity of a 3-(hydrazonomethyl) naphthalene-2-ol derivative, J. Biomol. Struct. Dyn. 41 (16) (2023) 7986–8001.
[10] H.A. Mahdy, et al., New theobromine derivatives inhibiting VEGFR-2: design, synthesis, antiproliferative, docking and molecular dynamics simulations, Future Med. Chem. 15 (14) (2023) 1233–1250.
[11] H. Elkady, et al., Synthesis, biological evaluation and computer-aided discovery of new thiazolidine-2, 4-dione derivatives as potential antitumor VEGFR-2 inhibitors, RSC Adv. 13 (40) (2023) 27801–27827.
[12] D. Panigrahy, et al., PPARγ ligands inhibit primary tumor growth and metastasis by inhibiting angiogenesis, J. Clin. Invest. 110 (7) (2002) 923–932.
[13] U. Bhanushali, et al., 5-Benzylidene-2, 4-thiazolidenedione derivatives: design, synthesis and evaluation as inhibitors of angiogenesis targeting VEGR-2, Bioorg. Chem. 67 (2016) 139–147.
[14] D.K. Shah, et al., Thiazolidinediones decrease vascular endothelial growth factor (VEGF) production by human luteinized granulosa cells in vitro, Fertil. Steril. 93 (6) (2010) 2042–2047.
[15] S. Takahashi, Vascular endothelial growth factor (VEGF), VEGF receptors and their inhibitors for antiangiogenic tumor therapy, Biol. Pharm. Bull. 34 (12) (2011) 1785–1788.
[16] P. Wu, T.E. Nielsen, M.H. Clausen, FDA-approved small-molecule kinase inhibitors, Trends Pharmacol. Sci. 36 (7) (2015) 422–439.
[17] M.S. Taghour, et al., Design, synthesis, anti-proliferative evaluation, docking, and MD simulations studies of new thiazolidine-2, 4-diones targeting VEGFR-2 and apoptosis pathway, PLoS One 17 (9) (2022) e0272362.
[18] M.S. Taghour, et al., Benzoxazole derivatives as new VEGFR-2 inhibitors and apoptosis inducers: design, synthesis, in silico studies, and antiproliferative evaluation, J. Enzym. Inhib. Med. Chem. 37 (1) (2022) 2063–2077.
[19] A. Elwan, et al., Modified benzoxazole-based VEGFR-2 inhibitors and apoptosis inducers: design, synthesis, and anti-proliferative evaluation, Molecules 27 (15) (2022) 5047.
[20] R.G. Yousef, et al., (E)-N-(3-(1-(2-(4-(2, 2, 2-trifluoroacetamido) benzoyl) hydrazono) ethyl) phenyl) nicotinamide: a novel pyridine derivative for inhibiting vascular endothelial growth factor receptor-2: synthesis, computational, and anticancer studies, Molecules 27 (22) (2022) 7719.
[21] E.B. Elkaeed, et al., The assessment of anticancer and VEGFR-2 inhibitory activities of a new 1 H-indole derivative: in silico and in vitro approaches, Processes 10 (7) (2022) 1391.
[22] K. Holmes, et al., Vascular endothelial growth factor receptor-2: structure, function, intracellular signalling and therapeutic inhibition, Cell. Signal. 19 (10) (2007) 2003–2012.
[23] A. Morabito, et al., Tyrosine kinase inhibitors of vascular endothelial growth factor receptors in clinical trials: current status and future directions, Oncol. 11 (7) (2006) 753–764.
[24] L.Q. Chow, S.G. Eckhardt, Sunitinib: from rational design to clinical efficacy, J. Clin. Oncol. 25 (7) (2007) 884–896.
[25] C.M. Adams, et al., The discovery of N-(1-Methyl-5-(trifluoromethyl)-1 H-pyrazol-3-yl)-5-((6-((methylamino) methyl) pyrimidin-4-yl) oxy)-1 H-indole-1-carboxamide (acrizanib), a VEGFR-2 inhibitor specifically designed for topical ocular delivery, as a therapy for neovascular age-related macular degeneration, J. Med. Chem. 61 (4) (2018) 1622–1635.
[26] X. Sheng, et al., A Phase I Clinical Trial of CM082 (X-82) in Combination with Everolimus for Treatment of Metastatic Renal Cell Carcinoma, American Society of Clinical Oncology, 2017.
[27] K.N. Moore, et al., Phase I, First-In-Human Trial of an Oral VEGFR Tyrosine Kinase Inhibitor (TKI) X-82 in Patients (Pts) with Advanced Solid Tumors, American Society of Clinical Oncology, 2012.
[28] Q.-Q. Xie, et al., Pharmacophore modeling studies of type I and type II kinase inhibitors of Tie2, J. Mol. Graph. Model. 27 (6) (2009) 751–758.
[29] K. Lee, et al., Pharmacophore modeling and virtual screening studies for new VEGFR-2 kinase inhibitors, Eur. J. Med. Chem. 45 (11) (2010) 5420–5427.
[30] R.N. Eskander, K.S. Tewari, Incorporation of anti-angiogenesis therapy in the management of advanced ovarian carcinoma—mechanistics, review of phase III randomized clinical trials, and regulatory implications, Gynecol. Oncol. 132 (2) (2014) 496–505.
[31] I.H. Eissa, et al., Design, molecular docking, in vitro, and in vivo studies of new quinazolin-4 (3H)-ones as VEGFR-2 inhibitors with potential activity against hepatocellular carcinoma, Bioorg. Chem. 107 (2021) 104532.
[32] S.A. El-Metwally, et al., Discovery of thieno [2, 3-d] pyrimidine-based derivatives as potent VEGFR-2 kinase inhibitors and anti-cancer agents, Bioorg. Chem. 112 (2021) 104947.
[33] V.A. Machado, et al., Synthesis, antiangiogenesis evaluation and molecular docking studies of 1-aryl-3-[(thieno [3, 2-b] pyridin-7-ylthio) phenyl] ureas: discovery of a new substitution pattern for type II VEGFR-2 Tyr kinase inhibitors, Bioorg. Med. Chem. 23 (19) (2015) 6497–6509.
[34] Z. Wang, et al., Dietary compound isoliquiritigenin inhibits breast cancer neoangiogenesis via VEGF/VEGFR-2 signaling pathway, PLoS One 8 (7) (2013) e68566.
[35] J. Dietrich, C. Hulme, L.H. Hurley, The design, synthesis, and evaluation of 8 hybrid DFG-out allosteric kinase inhibitors: a structural analysis of the binding interactions of Gleevec®, Nexavar®, and BIRB-796, Bioorg. Med. Chem. 18 (15) (2010) 5738–5748.
[36] M.K. Ibrahim, et al., Design, synthesis, molecular modeling and anti-hyperglycemic evaluation of quinazolin-4 (3H)-one derivatives as potential PPARγ and SUR agonists, Bioorg. Med. Chem. 25 (17) (2017) 4723–4744.
[37] W.M. Eldehna, et al., Novel 4/3-((4-oxo-5-(2-oxoindolin-3-ylidene) thiazolidin-2-ylidene) amino) benzenesulfonamides: synthesis, carbonic anhydrase inhibitory activity, anticancer activity and molecular modelling studies, Eur. J. Med. Chem. 139 (2017) 250–262.
[38] M.A. El-Zahabi, et al., Design, synthesis, and biological evaluation of new challenging thalidomide analogs as potential anticancer immunomodulatory agents, Bioorg. Chem. 104 (2020) 104218.
[39] A.A. Nasser, et al., Discovery of new pyrimidine-5-carbonitrile derivatives as anticancer agents targeting EGFR WT and EGFR T790M, Org. Biomol. Chem. 18 (38) (2020) 7608–7634.
[40] T. Mosmann, Rapid colorimetric assay for cellular growth and survival: application to proliferation and cytotoxicity assays, J. Immunol. Methods 65 (1–2) (1983) 55–63.
[41] B.A. Chabner, T.G. Roberts Jr., Chemotherapy and the war on cancer, Nat. Rev. Cancer 5 (1) (2005) 65–72.
[42] Y. Sun, et al., The influence of cell cycle regulation on chemotherapy, Int. J. Mol. Sci. 22 (13) (2021) 6923.
[43] C.A. Lipinski, et al., Experimental and computational approaches to estimate solubility and permeability in drug discovery and development settings, Adv. Drug Deliv. Rev. 23 (1–3) (1997) 3–25.
[44] K.V. Chuang, L.M. Gunsalus, M.J. Keiser, Learning molecular representations for medicinal chemistry: miniperspective, J. Med. Chem. 63 (16) (2020) 8705–8722.
[45] G. Moroy, et al., Toward in silico structure-based ADMET prediction in drug discovery 17 (1–2) (2012) 44–55.

[46] L.L.G. Ferreira, A.D. Andricopulo, ADMET modeling approaches in drug discovery, Drug Discov. Today 24 (5) (2019) 1157–1165.
[47] G. Idakwo, et al., A review on machine learning methods for in silico toxicity prediction, J. Environ. Sci. Health C Environ. Carcinog. Ecotoxicol. Rev. 36 (4) (2018) 169–191.
[48] D.Z. Husein, R. Hassanien, M. Khamis, Cadmium oxide nanoparticles/graphene composite: synthesis, theoretical insights into reactivity and adsorption study, RSC Adv. 11 (43) (2021) 27027–27041.
[49] T. Wang, D.Z. Husein, Novel synthesis of multicomponent porous nano-hybrid composite, theoretical investigation using DFT and dye adsorption applications: disposing of waste with waste, Environ. Sci. Pollut. Control Ser. 30 (4) (2023) 8928–8955.
[50] K. El-Adl, et al., Design, synthesis, molecular docking, anticancer evaluations, and in silico pharmacokinetic studies of novel 5-[(4-chloro/2, 4-dichloro) benzylidene] thiazolidine-2, 4-dione derivatives as VEGFR-2 inhibitors, Arch. Pharmazie 354 (2) (2021) 2000279.
[51] K. El-Adl, et al., Design, synthesis, and anti-proliferative evaluation of new quinazolin-4 (3H)-ones as potential VEGFR-2 inhibitors, Bioorg. Med. Chem. 29 (2021) 115872.
[52] M.M. Alanazi, et al., New bis ([1, 2, 4] triazolo)[4, 3-a: 3′, 4′-c] quinoxaline derivatives as VEGFR-2 inhibitors and apoptosis inducers: design, synthesis, in silico studies, and anticancer evaluation, Bioorg. Chem. 112 (2021) 104949.
[53] I.A. Osman, R.R. Ayyad, H.A. Mahdy, New pyrimidine-5-carbonitrile derivatives as EGFR inhibitors with anticancer and apoptotic activities: design, molecular modeling and synthesis, New J. Chem. 46 (24) (2022) 11812–11827.
[54] M.M. Alanazi, et al., Discovery of new quinoxaline-based derivatives as anticancer agents and potent VEGFR-2 inhibitors: design, synthesis, and in silico study, J. Mol. Struct. 1253 (2022) 132220.
[55] N.A. Alsaif, et al., Discovery of new VEGFR-2 inhibitors based on bis ([1, 2, 4] triazolo)[4, 3-a: 3', 4'-c] quinoxaline derivatives as anticancer agents and apoptosis inducers, J. Enzym. Inhib. Med. Chem. 36 (1) (2021) 1093–1114.
[56] M.M. Alanazi, et al., Design, synthesis, docking, ADMET studies, and anticancer evaluation of new 3-methylquinoxaline derivatives as VEGFR-2 inhibitors and apoptosis inducers, J. Enzym. Inhib. Med. Chem. 36 (1) (2021) 1760–1782.
[57] T. Slater, B. Sawyer, U. Sträuli, Studies on succinate-tetrazolium reductase systems: III. Points of coupling of four different tetrazolium salts III. Points of coupling of four different tetrazolium salts, Biochim. Biophys. Acta 77 (1963) 383–393.
[58] A. Van de Loosdrecht, et al., A tetrazolium-based colorimetric MTT assay to quantitate human monocyte mediated cytotoxicity against leukemic cells from cell lines and patients with acute myeloid leukemia 174 (1–2) (1994) 311–320.
[59] M.C. Alley, et al., Feasibility of drug screening with panels of human tumor cell lines using a microculture tetrazolium assay 48 (3) (1988) 589–601.
[60] E.B. Elkaeed, et al., In silico, in vitro VEGFR-2 inhibition, and anticancer activity of a 3-(hydrazonomethyl) naphthalene-2-ol derivative, J. Biomol. Struct. Dyn. (2022) 1–16.
[61] I.H. Eissa, et al., Design and discovery of new antiproliferative 1, 2, 4-triazin-3 (2H)-ones as tubulin polymerization inhibitors targeting colchicine binding site, Bioorg. Chem. 112 (2021) 104965.
[62] F. Taverna, et al., Biological quality control for extracorporeal photochemotherapy: assessing mononuclear cell apoptosis levels in ECP bags of chronic GvHD patients, J. Clin. Apher. 30 (3) (2015) 162–170.
[63] W.M. Eldehna, et al., Design, synthesis, in vitro biological assessment and molecular modeling insights for novel 3-(naphthalen-1-yl)-4, 5-dihydropyrazoles as anticancer agents with potential EGFR inhibitory activity, Sci. Rep. 12 (1) (2022) 12821.
[64] I. Arranz-Valsero, et al., IL-6 as a corneal wound healing mediator in an in vitro scratch assay, Exp. Eye Res. 125 (2014) 183–192.
[65] M.S. Taghour, et al., Design and synthesis of thiazolidine-2, 4-diones hybrids with 1, 2-dihydroquinolones and 2-oxindoles as potential VEGFR-2 inhibitors: in-vitro anticancer evaluation and in-silico studies, J. Enzym. Inhib. Med. Chem. 37 (1) (2022) 1903–1917.
[66] M.M. Alanazi, et al., New quinoxaline-based VEGFR-2 inhibitors: design, synthesis, and antiproliferative evaluation with in silico docking, ADMET, toxicity, and DFT studies, RSC Adv. 11 (48) (2021) 30315–30328.
[67] E.B. Elkaeed, et al., Discovery of new VEGFR-2 inhibitors: design, synthesis, anti-proliferative evaluation, docking, and MD simulation studies, Molecules 27 (19) (2022) 6203.
[68] M.S. Alesawy, et al., In silico studies of some isoflavonoids as potential candidates against COVID-19 targeting human ACE2 (hACE2) and viral main protease (Mpro), Molecules 26 (9) (2021) 2806.
[69] H. Elkady, et al., New benzoxazole derivatives as potential VEGFR-2 inhibitors and apoptosis inducers: design, synthesis, anti-proliferative evaluation, flowcytometric analysis, and in silico studies, J. Enzym. Inhib. Med. Chem. 37 (1) (2022) 403–416.
[70] I.H. Eissa, et al., Diphenylurea derivatives for combating methicillin-and vancomycin-resistant Staphylococcus aureus, Eur. J. Med. Chem. 130 (2017) 73–85.
[71] I.H. Eissa, et al., In silico exploration of potential natural inhibitors against SARS-Cov-2 nsp10, Molecules 26 (20) (2021) 6151.
[72] M.J. Abraham, et al., GROMACS: high performance molecular simulations through multi-level parallelism from laptops to supercomputers 1 (2015) 19–25.
[73] E.B. Elkaeed, et al., A multistage in silico study of natural potential inhibitors targeting SARS-CoV-2 main protease, Int. J. Mol. Sci. 23 (15) (2022) 8407.
[74] S. Jo, et al., CHARMM-GUI PDB Manipulator for Advanced Modeling and Simulations of Proteins Containing Nonstandard Residues, vol. 96, 2014, pp. 235–265.
[75] J. Lee, et al., CHARMM-GUI input generator for NAMD, GROMACS, AMBER, OpenMM, and CHARMM/OpenMM simulations using the CHARMM36 additive force field 12 (1) (2016) 405–413.
[76] T. Tuccinardi, What is the current value of MM/PBSA and MM/GBSA methods in drug discovery? Exp. Opin. Drug Discov. 16 (11) (2021) 1233–1237.
[77] M.S. Valdés-Tresanco, et al., gmx_MMPBSA: a new tool to perform end-state free energy calculations with GROMACS 17 (10) (2021) 6281–6291.
[78] C. Bouysset, S. Fiorucci, ProLIF: a library to encode molecular interactions as fingerprints, J. Cheminf. 13 (2021) 1–9.
[79] S. Salentin, et al., PLIP: fully automated protein–ligand interaction profiler, Nucleic Acids Res. 43 (W1) (2015) W443–W447.
[80] T. Tubiana, et al., TTClust: a versatile molecular simulation trajectory clustering program with graphical summaries, J. Chem. Inf. Model. 58 (11) (2018) 2178–2182.
[81] A. Amadei, A.B. Linssen, H.J. Berendsen, Essential dynamics of proteins, Proteins: Struct., Funct., Bioinf. 17 (4) (1993) 412–425.
[82] E. Papaleo, et al., Free-energy landscape, principal component analysis, and structural clustering to identify representative conformations from molecular dynamics simulations: the myoglobin case, J. Mol. Graph. Model. 27 (8) (2009) 889–899.
[83] G.G. Maisuradze, D.M. Leitner, Free energy landscape of a biomolecule in dihedral principal component space: sampling convergence and correspondence between structures and minima, Proteins: Struct., Funct., Bioinf. 67 (3) (2007) 569–578.
[84] B. Hess, Similarities between principal components of protein dynamics and random diffusion, Phys. Rev. 62 (6) (2000) 8438.
[85] E.B. Elkaeed, et al., Design, synthesis, docking, DFT, MD simulation studies of a new nicotinamide-based derivative: in vitro anticancer and VEGFR-2 inhibitory effects, Molecules 27 (14) (2022) 4606.